The AICC2023 chronological framework and associated timescale for the EPICA Dome C ice core.

Marie Bouchet[1], Amaëlle Landais[1], Antoine Grisart[1], Frédéric Parrenin[2], Frédéric Prié[1], Roxanne Jacob[1], Elise Fourré[1], Emilie Capron[2], Dominique Raynaud[2], Vladimir Ya Lipenkov[3], Marie-France Loutre[4,5], Thomas Extier[6], Anders Svensson[7], Etienne Legrain[2], Patricia Martinerie[2], Markus Leuenberger[8], Wei Jiang[9], Florian Ritterbusch[9], Zheng-Tian Lu[9], Guo-Min Yang[9].

[1]Laboratoire des Sciences du Climat et de l'Environnement, LSCE-IPSL, CEA-CNRS-UVSQ, Univ. Paris-Saclay, 91190 Gif-sur-Yvette, France.

[2]Univ. Grenoble Alpes, CNRS, INRAE, IRD, Grenoble INP, IGE, 38000 Grenoble, France.

[3]Arctic and Antarctic Research Institute, 199397 St. Petersburg, Russia.

[4]PAGES International Project Office University of Bern, 3012 Bern, Switzerland.

[5]Université catholique de Louvain, B-1348 Louvain-la-Neuve, Belgium.

[6]Univ. Bordeaux, CNRS, Bordeaux INP, EPOC, UMR 5805, 33600 Pessac, France.

[7]Niels Bohr Institute, University of Copenhagen, 2100 Copenhagen, Denmark.

[8]Physics Institute, University of Bern, 3012 Bern, Switzerland.

[9]Hefei National Laboratory, University of Science and Technology of China, Hefei, 230026, China.

Correspondance to: Marie Bouchet (marie.bouchet@lsce.ipsl.fr)

Abstract. The EPICA (European Project for Ice Coring in Antarctica) Dome C (EDC) ice core drilling in East Antarctica reaches a depth of 3260 m. The reference EDC chronology, the AICC2012 (Antarctic Ice Core Chronology 2012), provides an age vs depth relationship covering the last 800 kyr (thousands of years) with an absolute uncertainty rising up to 8,000 years at the bottom of the ice core. The origins of this relatively large uncertainty are twofold: (1) the $\delta^{18}O_{atm}$, $\delta O_2/N_2$ and total air content (TAC) records are poorly resolved and show large gaps over the last 800 kyr and (2) large uncertainties are associated with their orbital targets. Here, we present new highly resolved $\delta^{18}O_{atm}$, $\delta O_2/N_2$ and $\delta^{15}N$ measurements for EDC ice core covering the last five glacial - interglacial transitions, a new low resolution TAC record over the period 440-800 ka BP (thousand years before 1950), as well as novel absolute ^{81}Kr ages. We have compiled chronological and glaciological information including novel orbital age markers from new data on EDC ice core as well as accurate firn modeling estimates in a Bayesian dating tool to construct the new AICC2023 chronology. For the first time, three orbital tools are used simultaneously. Hence, it is possible to observe that they are consistent with each other and with the other age markers over most of the last 800 kyr (70 %). This, in turn, gives us confidence in the new AICC2023 chronology. The average uncertainty of the ice chronology is reduced from 1,700 years to 900 years in AICC2023 over the last 800 kyr (1σ). The new timescale diverges from AICC2012 and suggests age shifts reaching 3,800 years towards older ages over Marine Isotopes Stages (MIS) 5, 11 and 19. But, the coherency between the new AICC2023 timescale and independent chronologies of other archives (Italian Lacustrine succession from Sulmona Basin, Dome Fuji ice core and northern Alpine speleothems) is improved by 1,000 to 2,000 years over these time intervals.

1 Introduction

1.1 Building age scales for deep polar ice cores

1.1.1 Motivation

Deep polar ice cores are unique archives of past climate and their investigation is valuable to study mechanisms governing the Earth's climate variations. Precise chronologies are key to identify the successions and lengths of climatic events, along with exploring phase relationships between the external forcing (changes in the Earth's orbit) and the diverse climatic responses (variations in temperature and atmospheric greenhouse gas concentrations). To date ice cores, we need to construct two separate chronologies: one for the ice and one for the younger air trapped in bubbles. Due to the thinning of ice horizontal layers as we go down in depth, a wide timespan of paleoclimatic information is stored within the deepest part of the ice sheet. Therefore, many of the ice core community's ongoing efforts focus on improving deep ice core timescales for ice and gas phases, as well as extending them further back in time (Crotti et al., 2021; Oyabu et al., 2022). Ice cores drilled at sites characterized by a high accumulation rate of snow at the surface (10 to 30 cm/year) can be dated by counting ice layers deposited year after year (Svensson et al., 2008; Sigl et al., 2016). On the contrary, East Antarctica sites are associated with very low accumulation rates (1 to 5 cm/year) which prevent annual layers from being identified and counted. As a consequence, chronologies of ice cores at low-accumulation sites are commonly established using ice flow and accumulation models (Nye, 1959; Schwander et al., 2001), then tied up with chronological and glaciological constraints (Veres et al., 2013; Bazin et al., 2013; Parrenin et al., 2017).

1.1.2 Glaciological modeling

Glaciological modeling has been historically used to date Greenlandic and Antarctic ice cores. A unidimensional ice flow model was first applied to the Camp Century ice core (Dansgaard and Johnsen, 1969), and later to other ice cores such as the ones drilled at EPICA Dome C (EDC) and Dome Fuji (EPICA members, 2004; Parrenin et al., 2007). First, water isotopes (δD or δ^{18}O) measurements provide estimates of past evolution of the accumulation rate of snow and temperature at surface. Then, an ice flow model (Parrenin et al., 2004) takes as inputs past accumulation together with a vertical velocity depth-profile through the ice sheet to determine the thinning of annual snow/ice layers in time, and therefore the ice timescale. This approach is very sensitive to some poorly known parameters including boundary conditions such as bedrock topography, geothermal properties or subglacial sliding. For this reason, the glaciological modeling approach is complemented with chronological constraints (gas or ice age known at certain depth levels).

1.1.3 Chronological constraints derived from measurements

Chronological constraints obtained either by measurement of radionuclides or by synchronization to a curve of reference are established for both ice and gas timescales. For building long chronologies, some time constraints can be obtained from the ^{10}Be series measured in ice. The ^{10}Be cosmogenic nuclide is produced at different rate depending on the solar activity and its arrival on Earth is modulated by the strength of the Earth's magnetic field (Yiou et al., 1997; Raisbeck et al., 2007; Heaton et al., 2021). Some links hence exist between ^{10}Be flux and precisely dated magnetic events such as the Laschamp excursion, an abrupt decline in the geomagnetic field magnitude occurring at about 41 ka BP and visible as a positive excursion in the ^{10}Be flux records in ice cores (Lascu et al., 2016; Raisbeck et al., 2017). ^{40}Ar measurements in the gas phase of Antarctic ice cores also provide

dating constraints for old ice, especially for non-continuous stratigraphic sequences (Yan et al., 2019). ^{40}Ar is produced in solid earth by the radioactive decay of ^{40}K leading to an increasing concentration of ^{40}Ar in the atmosphere at a rate of 0.066 ± 0.006 ‰ Myr^{-1} (Bender et al., 2008). Recently, the possibility of measuring ^{81}Kr in ice samples of a few kg gave a new absolute dating tool for ice cores (Jiang et al., 2020). ^{81}Kr is a radioactive isotope that is suitable for dating ice cores in the range from 0.03 to 1.3 Ma BP (million years before 1950), making it perfectly adapted for Antarctic ice core dating (Buizert et al., 2014; Crotti et al., 2021).

To further constrain oldest ice core chronologies, the so-called "orbital dating" tools are also used. These tools consist in aligning some tracers measured in ice cores to the Earth orbital series, called targets, whose fluctuations in time are accurately calculated from the known variations of orbital parameters (Berger, 1978; Laskar et al., 2011). The synchronization of the orbital tracer with its target provides ice or gas age constraints. So far, three orbital dating tools have been developed δ^{18}O of O$_2$ (δ^{18}O$_{atm}$), δO$_2$/N$_2$ and total air content (TAC). The δ^{18}O$_{atm}$ was typically aligned with the precession parameter (or with the 21st June insolation at 65°North) delayed by 5,000 years because such a lag between δ^{18}O$_{atm}$ and its orbital target was observed during the last deglaciation (Shackleton, 2000; Dreyfus et al., 2007). However, variations in the phasing between δ^{18}O$_{atm}$ and precession have been suspected (Jouzel et al., 2002) and identified since (Bazin et al., 2016). In particular, millennial-scale events (as Heinrich-like events) occurring during deglaciations have been shown to delay the response of δ^{18}O$_{atm}$ to orbital forcing (Extier et al., 2018a). Because there was a significant unpredictability in the lag between δ^{18}O$_{atm}$ and its orbital target, a large uncertainty in the δ^{18}O$_{atm}$ based tie points (up to 6,000 years) was assigned in the construction of the AICC2012 (Antarctic Ice Core Chronology 2012, Bazin et al., 2013). To improve the accuracy of the gas timescale, Extier et al. (2018a) rather aligned the variations of δ^{18}O$_{atm}$ to the δ^{18}O$_{calcite}$ recorded in absolute dated East Asian speleothems between 640 and 100 ka BP. Indeed, the two records show similar orbital (related to the 21st July insolation at 65° North) and millennial variabilities, which may correspond to southward shifts in the InterTropical Convergence Zone (ITCZ) position, themselves linked to Heinrich-like events as supported by the modeling study of Reutenauer et al. (2015).

In parallel, Bender (2002) observed that the elemental ratio δO$_2$/N$_2$ of air trapped in Vostok ice core appears to vary in phase with the 21st of December insolation at 78° South (Vostok latitude) between 400 and 160 ka BP. Subsequent observations led Bender (2002) to assert that local summer solstice insolation affects near-surface snow metamorphism and that this imprint is preserved as snow densifies in the firn and, later on, affects the ratio δO$_2$/N$_2$ measured in air bubbles formed at the lock-in-zone. Wiggle matching between δO$_2$/N$_2$ and local summer solstice insolation has been used to construct orbital timescales for Dome Fuji, Vostok and EDC ice cores reaching back 360, 400 and 800 ka BP respectively, with a chronological uncertainty for each δO$_2$/N$_2$ tie point estimated between 250 and 4,000 years (Kawamura et al., 2007; Suwa and Bender, 2008; Bazin et al., 2013; Oyabu et al., 2022). Finally, Raynaud et al. (2007) found very similar spectral properties between the TAC record of EDC and the integrated summer insolation at 75° South (ISI) obtained by a summation over a year of all daily local insolation above a certain threshold over the last 440 kyr. As for δO$_2$/N$_2$, these similarities may be explained by the insolation imprint in near-surface snow well preserved down to the lock-in zone, where it could affect the air content in deep ice although the physical mechanisms involved during the snow and firn densification for δO$_2$/N$_2$ and TAC are likely different (Lipenkov et al., 2011). Lately, Bazin et al. (2013) made use of TAC to constrain Vostok and EDC ice core chronologies back to 430 ka BP with an uncertainty for each TAC tie point varying between 3,000 and 7,000 years. Although these three orbital tools complement each other (TAC and

116 $\delta O_2/N_2$ inferred ages agree within less than 1,000 years between 390 and 160 ka BP for the Vostok ice core,

117 Lipenkov et al., 2011), they hardly ever have been employed together. Plus, they are often associated with large

118 uncertainties (reaching 7,000 years) which lie in the choice of the appropriate orbital target, in its alignment with

119 ice core records that can be ambiguous during periods of low eccentricity in the Earth's orbit (leading to low-

120 amplitude insolation variations) and in the poor quality of the signals measured in the deepest section of the cores.

121 To connect ice and gas timescales, the estimation of the lock-in-depth (LID), indicating the lowest depth where

122 the air is trapped in enclosed bubbles and diffusivity becomes effectively zero (Buizert et al., 2013), is used to

123 calculate the ice/gas age difference. Measurements of $\delta^{15}N$ from N_2 yield a first estimate of this depth and the LID

124 can also be calculated with firn densification modeling (Goujon et al., 2003; Bréant et al., 2017).

125 For many years, each polar ice core was characterized by its singular timescale which was not naturally

126 consistent with other ice core timescales. To address this issue, other measurements provide relative dating

127 constraints (stratigraphic links) improving the coherency between timescales of ice cores from both hemispheres.

128 The synchronization of globally well-mixed atmospheric methane ice core records gives tie points with an accuracy

129 of a few decades to several centuries (60-1,500 years) (Lemieux-Dudon et al., 2010; Epifanio et al., 2020). Climate

130 independent events, such as large volcanic eruptions, can be observed in ice cores from Greenland and Antarctica

131 via singular patterns of the distribution of sulfate. Identification of these deposits permits to precisely synchronize

132 several ice cores (within 5 to 150 years) (Svensson et al., 2020).

1.1.4 Bayesian dating tools

134 In order to integrate stratigraphic matching, independent synchronization and absolute dating constraints as well

135 as glaciological modeling to produce coherent ice core chronologies, researchers developed Bayesian dating tools

136 such as Datice (Lemieux-Dudon et al., 2010), IceChrono1 (Parrenin et al., 2015) and Paleochrono (Parrenin et al.,

137 2021). These tools use an inverse method combining all chronological information to provide a coherent age scale

138 for several ice cores. These probabilistic tools adjust prior estimates of ice and gas chronologies built with a

139 glaciological model (background scenario) so that they respect chronological constraints.

140 Here we focus on the chronology of the EDC deep ice core. The EPICA project provided two cores in East

141 Antarctica including one at Dome C (EDC, 2004). The second (and final) drilling attempt at Dome C gave the

142 3260 m long EDC99 core, whose drilling has been willingly stopped at 15 m above bedrock due to expected

143 presence of melt water. EDC furnishes the oldest continuous ice core record so far, covering the last 800 kyr

144 (EPICA community members, 2004; Jouzel et al., 2007).

1.2 The AICC2012 chronology

146 Bazin et al. (2013) and Veres et al. (2013) used the probabilistic dating tool Datice to establish the coherent

147 AICC2012 chronology back to 800 ka BP for five ice cores including EDC, Vostok, EPICA Dronning Maud Land

148 ice core (EDML), North Greenland Ice core Project (NGRIP) and Talos Dome Ice core (TALDICE). To determine

149 EDC age scale, they used various orbital dating constraints including: 39 tie points attached to a 6,000 years

150 uncertainty derived from $\delta^{18}O_{atm}$ tuning to 5,000 years delayed precession between 800 and 300 ka BP, 20 tie

151 points associated with a 4,000 years uncertainty from $\delta O_2/N_2$ alignment to local summer solstice insolation

152 between 800 and 300 ka BP, and 14 tie points linked to an uncertainty between 3,000 and 7,000 years using TAC

153 synchronized to integrated summer insolation between 430 and 0 ka BP. However, due to the lack of data for the

154 orbital dating approach, AICC2012 1σ uncertainty is of 1,700 years on average, reaching 8,000 years at the bottom

155 of the core. The origins of AICC2012 uncertainty can be divided in the following points: (i) some inherent

156 dissimilarities between $\delta^{18}O_{atm}$, $\delta O_2/N_2$ and TAC series and their curve-shaped orbital target; (ii) discontinuity and

157 poor quality of the $\delta O_2/N_2$ and TAC records; (iii) uncertainty on the phasing between $\delta^{18}O_{atm}$ and precession; (iv)

158 poor constraint on the LID scenario due to a disagreement between $\delta^{15}N$ data and firn modeling estimates (Bréant

159 et al., 2017).

1.3 The new AICC2023 chronology

161 It is now possible to address each source of uncertainty thanks to recent advances: (i) Since AICC2012, the $\delta^{18}O_{atm}$

162 and TAC records have been extended, now covering the last 800 kyr (Extier et al., 2018b). In addition, new highly

163 resolved $\delta^{18}O_{atm}$ and $\delta O_2/N_2$ measurements are available over several glacial terminations (TII, III, IV, V and VI)

164 (Grisart, 2023). (ii) Extier et al. (2018a) recently suggested a $\delta^{18}O_{atm}$ based timescale using $\delta^{18}O_{calcite}$ of East Asian

165 speleothems as an alternative tuning target to precession. This choice reduces the chronological uncertainty

166 between 640 and 100 ka BP. (iii) Finally, new highly resolved $\delta^{15}N$ data covering the Terminations II to VI are

167 available (Grisart, 2023). In parallel, firn densification models have been progressively improved and the model

168 described in Bréant et al. (2017) can be employed to estimate LID evolution in the past when $\delta^{15}N$ data are still

169 missing.

170   In this work, we implement new absolute age constraints spanning the last 800 kyr derived from [81]Kr measured

171 in air trapped in EDC ice core as well as new orbital age constraints obtained by synchronizing up-to-date EDC

172 records with their orbital target. We combine these data to recent volcanic matching and methane records

173 synchronization which provide additional stratigraphic links, relating EDC to other ice cores over the past 122 kyr

174 (Baumgartner et al., 2014; Svensson et al., 2020). Finally, we propose the new chronology AICC2023 with reduced

175 chronological uncertainties. AICC2023 is recommended as the new official age scale for the EPICA ice cores by

176 the EPICA Scientific Steering Committee (Wolff, 2023).

2   Methods

2.1 Dating strategy

179   The Paleochrono Python software is a probabilistic dating tool similar to Datice and Icechrono1 with

180 improved mathematical, numerical and programming capacities (Parrenin et al., 2021). The dating strategy of

181 Paleochrono relies on the Bayesian inference of three glaciological functions forming the input background

182 scenario: accumulation rate (A), thinning of annual ice layers (τ) and Lock-In-Depth (LID). The three variables

183 evolve along the ice core depth z and are used to estimate the ice (ψ) and gas (χ) age profiles as follows:

$$\psi(z) = \int_{0}^{z} \frac{D(z')}{\tau(z')A(z')}dz' \tag{1}$$

$$\chi(z) = \psi\big(z - \Delta depth(z)\big) \tag{2}$$

$$\int_{z-\Delta depth(z)}^{z} \frac{D(z')}{\tau(z')}dz' = LID(z) \times \frac{D}{\tau}\bigg|_{firn}^{0} \tag{3}$$

where D is the relative density of the snow/ice and $\left.\frac{D}{\tau}\right|^0_{firn}$ the average value of $\frac{D}{\tau}$ in the firn when the air particle was at the lock-in-depth (this parameter is usually ~0.7, Parrenin et al., 2012). The age scales are further constrained to respect chronological constraints identified from observations. To specify the credibility of the background scenario for the age scales and the chronological constraints, the glaciological functions (accumulation, thinning and LID) and the chronological information can be mathematically expressed as probability densities which are presumed to be Gaussian and independent (i.e. decorrelated between them). Thus, the inference is based on the Least Square optimisation method (implying all probability densities Gaussian). It is numerically solved using the Trust Region algorithm (assuming that the model is roughly linear around the solution) and the Jacobian of the model is evaluated analytically for an improved computation time. As a result, the best adjustment between the background scenario and chronological observations is found, providing the most probable scenario as a posterior evaluation of the three glaciological functions and hence chronologies for ice and air. For each ice core, the input files for Paleochrono are the following: (i) the background values of the three glaciological functions with depth, (ii) gas and ice stratigraphic links, (iii) gas and ice dated horizons, which are tie points derived for one core from absolute and synchronization dating methods, (iv) gas and ice intervals of known durations and (v) depth difference estimates between the same event recorded in the gas and ice matrix (Δdepth). Specific relative or absolute uncertainties are attached to each of these parameters in each input file.

In this study, we added numerous gas and ice dated horizons for EDC as well as an updated background scenario for the LID. Then, to construct a new chronology for EDC ice core that is consistent with the timescales of Vostok, TALDICE, EDML and NGRIP ice cores, we followed the same strategy as for the construction of AICC2012. Glaciological background parameters and dating constraints for Vostok, TALDICE, EDML, NGRIP and EDC drillings are compiled in one run of Paleochrono to obtain AICC2023. Vostok, TALDICE, EDML and NGRIP background parameters and dating constraints are extracted from Bazin et al. (2013) except for: (i) new Vostok gas age constraints determined from the alignment of $\delta^{18}O_{atm}$ and East Asian $\delta^{18}O_{calcite}$ records as for EDC (see supplementary Fig. S10), (ii) new TALDICE background parameters and age constraints from Crotti et al. (2021) and (iii) corrected LID background scenarios for Vostok and EDML sites (see supplementary Fig. S11). In order to prevent any confusion with reference ice core timescales, the new AICC2023 chronology for NGRIP is compelled to respect exactly the layer-counted GICC05 timescale through absolute tie points placed at one-meter intervals over the last 60 kyr (Andersen et al., 2006). For this reason, we did not use the methodology described by Lemieux-Dudon et al. (2015) which implemented layer counting as a constraint on the duration of events in the dating tool, inducing a slight shift (maximum 410 years) on the AICC2012 timescale. The resulting Paleochrono experiment provides the new official chronology AICC2023 for the EDC ice core. The contingent timescales obtained for the four other sites are not the subject of this study but are also provided (see Data Availability section). We acknowledge the exclusion of the WAIS (West Antarctic Ice Sheet) Divide ice core (WDC) from the construction of the AICC2023 age scale as for AICC2012 age scale. Over the last 60 kyr, though, we recommend the use of timescales tied to the WAIS Divide 2014 age model (WD2014, Buizert et al., 2015; Sigl et al., 2016). A correspondence between AICC2012, AICC2023 and WD2014 age models based on the volcanic synchronization of WDC and EDC using sulfate data (Buizert et al., 2018) is provided over the 0-58 ka BP period (that is to say for the section above the depth of 915 m for the EDC ice core, see Data Availability section).

2.2 Analytical method

2.2.1 $\delta^{18}O_{atm}$, $\delta O_2/N_2$ and $\delta^{15}N$

The measurements of the isotopic and elemental compositions of O_2 and N_2 were performed by Grisart (2023) at LSCE following the method described by Bréant et al. (2019) and Extier et al. (2018a). The air trapped in the EDC ice core is extracted using the semi-automatic line which eliminates CO_2 and H_2O. 30 to 40 g samples are prepared in a cold environment (-20°C), their exterior layer (3-5mm) is removed so that there is no exchange with atmospheric air and each sample is cut in two replicates. Each day, three ice samples (and replicates) are placed in six flasks and the atmospheric air is evacuated from the flasks. Samples are then melted and left at ambient temperature for approximately 1h30 in order to extract the air trapped in ice samples. The extracted air is then cryogenically trapped within a dedicated manifold immersed in liquid helium (Bazin et al., 2016). Along the way to the cryogenic trap, the air goes through cold traps to remove CO_2 and H_2O. Two additional samples containing exterior modern air are processed through the same line every day for calibration and for monitoring the analytical set-up. Lastly, the $\delta^{15}N$, $\delta^{18}O$ of O_2 and $\delta O_2/N_2$ of each sample are measured by a dual inlet Delta V plus (Thermo Electron Corporation) mass spectrometer.

Classical corrections are applied on the measurements (pressure imbalance, chemical slopes, as per Landais et al., 2003). In addition, $\delta^{15}N$ data are used to get the values of atmospheric $\delta^{18}O$ of O_2 and $\delta O_2/N_2$ after gravitational fractionation occurred in the firn, so that $\delta^{18}O_{atm} = \delta^{18}O$ of $O_2 - 2 \times \delta^{15}N$ and $\delta O_2/N_{2(corr)} = \delta O_2/N_{2(raw)} - 4 \times \delta^{15}N$ (Landais et al., 2003; Bazin et al., 2016; Extier et al., 2018a). Note that our samples were stored at -50°C since drilling to minimize gas loss effect. As a consequence, no correction for gas loss was applied (see Sect. 1 in the Supplementary Material) and if gas loss may explain a slight scattering in the data, the peak positions are not affected.

Existing and new EDC data are compiled in Table 1. The resulting data set pooled standard deviations for the new measurements are of 0.006, 0.03 and 0.4 ‰ for $\delta^{15}N$, $\delta^{18}O_{atm}$ and $\delta O_2/N_2$ respectively.

Table 1. **Information on isotopic and elemental compositions measured in air trapped in EDC ice core**. *Details on storage and measurement conditions of $\delta O_2/N_2$ are available in Sect. 1 in the Supplementary Material.

	$\delta^{18}O_{atm}$			$\delta O_2/N_2$ *			$\delta^{15}N$		
	Depth (m)	AICC2012 gas age (ka BP)	Resolution (kyr)	Depth (m)	AICC2012 ice age (ka BP)	Resolution (kyr)	Depth (m)	AICC2012 gas age (ka BP)	Resolution (kyr)
AICC2012									
Dreyfus et al. (2007, 2008, 2010); Landais et al. (2012); Bazin et al. (2013)	2479 - 3260	300 - 800	1 - 1.5	2480 - 3260	300 - 800	2.5	346 - 578	11 - 27	0.35 - 0.38
							1090 - 1169	75 - 83	1.4
							1389 - 3260	100 - 800	2.4
Bazin et al. (2016)	1300 - 1903	90 - 160	1.1	1300 - 1903	93 - 163	2.37			
	2657 - 3260	370 - 800		2595 - 3260	340 - 800	2.08			
Extier et al. (2018b, 2018c)	1872 - 2665	153 - 374	0.16 - 0.7	1904 - 2562	164 - 332	2 - 2.5			

Bréant et al. (2019)							1904 - 2580	160.2 - 334.5	1.013
This work (Grisart, 2023)	1489.95 - 1832.6	108.0 - 136.3	0.333	1489.95 - 1832.6	111.4 - 148.9	0.441	1489.95 - 1832.6	108.0 - 136.3	0.333
	1995.95 - 2350.15	180.6 - 255.8	0.437	1995.95 - 2350.15	183.9 - 259.6	0.437	1995.95- 2350.15	180.6 - 255.8	0.437
	2555.85 - 2633.4	328.3 - 346.8	0.356	2555.85 - 2633.4	330.5 - 360.6	0.579	2555.85 - 2633.4	328.3 - 346.8	0.356
	2744.5 - 2797.85	408.7 - 445.9	0.744	2744.5 - 2797.85	410.7 - 449.6	0.779	2744.5 - 2797.85	408.7 - 445.9	0.744
	2873.75 - 2910.6	508.1 - 535.6	1.375	2873.75 - 2910.6	511.3 - 539.3	1.401	2873.75 - 2910.6	508.1 - 535.6	1.375

2.2.2 Total Air Content

The TAC record has been measured in the entire EDC ice core at the IGE (Institute of Environmental Geosciences) following the barometric method firstly described by Lipenkov et al. (1995). The TAC record measured in the younger part of the core (400 – 0 ka BP) has been published in Raynaud et al. (2007) (Table 2). TAC estimates need to be corrected for cut-bubble effect. After correction, the uncertainty in TAC values is of about 1 % and the analysis replicability is better than 1 %.

Table 2. Information on TAC measurements in EDC ice core.

	TAC		
	Depth (m)	AICC2012 ice age (ka BP)	Resolution (kyr)
AICC2012 (Raynaud et al., 2007)	115 - 2800	0 - 440	2.000
Unpublished	2800 - 3260	440 - 800	2.000

2.2.3 ^{81}Kr extraction and analysis

The analytical method is the same as described by Crotti et al. (2021). Three ice samples of 6 kg each are taken from the bottom part of EDC and a slight shaving (1 mm) of the external layer is performed before processing. The air extraction is performed through a manual extraction line following the protocol described in Tian et al. (2019). The ice sample is placed in a 40 L stainless-steel chamber. The atmospheric air is pumped while the chamber is kept at -20°C. The air is then slowly extracted, passing through a water trap, and compressed in a stainless-steel cylinder. The three cylinders are sent to the University of Sciences and Technology of China (USTC, Hefei, China) for Krypton extraction and analysis. Krypton extraction is performed after the methodology of Dong et al. (2019) who set up an automated system for dual separation of Argon and Krypton, composed of a Titanium getter module followed by a Gas-Chromatography separator module. The extracted Krypton is analyzed by the Atom Trap Trace Analysis (ATTA) instrument set up at the Laser Laboratory for Trace Analysis and Precision Measurement (LLTAPM, USTC, Hefei, China), giving the ^{81}Kr abundance R_{81} in the sample. R_{81} is determined by the number of counted ^{81}Kr atoms in the sample as compared to the atmospheric reference. The anthropogenic

272 ^{85}Kr is measured simultaneously with ^{81}Kr to control any present-day air contamination. Here, the ^{85}Kr abundance

273 measured in ice samples is inferior to the detection limit, so contamination has occurred.

274 From the ^{81}Kr abundance, it is possible to estimate ^{81}Kr radioactive decay and to calculate the ice samples

275 age. As a noble gas isotope, ^{81}Kr is globally mixed in the atmosphere and its decay cannot be affected by complex

276 chemical reactions (Lu et al., 2014). ^{81}Kr half-life ($t_{1/2}$) is estimated to $\simeq 229\pm11$ kyr (Baglin, 2008). ^{81}Kr age

277 can be calculated as per the following equation:

$$\text{age} = -\frac{t_{\frac{1}{2}}}{\ln(2)} \times \ln(R_{81}) \tag{4}$$

279 The atmospheric abundance of ^{81}Kr is not constant in the past and its value is corrected using reconstruction of the

280 geomagnetic field intensity (Zappala et al., 2020). The error in ^{81}Kr age estimates is estimated from the statistical

281 error of atom counting, from the uncertainty in ^{81}Kr half-life (inducing a systematic age error) and from the size

282 of the sample (larger sample resulting in a smaller uncertainty).

283 **2.3 Firn model**

284 Firn densification models have been progressively improved over the years (Herron and Langway, 1980;

285 Alley, 1987; Arthern et al., 2010; Ligtenberg et al., 2011; Kuipers Munneke et al., 2015; Oraschewski and Grinsted,

286 2022). While these models generally explain well the evolution of δ^{15}N in time through changes in the LID, they

287 fail to reproduce values of δ^{15}N in some regions including coastal areas and cold and low accumulation sites such

288 as EDC (Capron et al., 2013). This disagreement can be explained by an inaccurate estimate of glacial temperature

289 and accumulation rate at surface (Buizert et al., 2021) and/or by the impossibility to tune empirical firn models to

290 sites with no present-day equivalent in terms of temperature and accumulation rate (Dreyfus et al., 2010; Capron

291 et al., 2013). Lately, the firn model described in Bréant et al. (2017) has been developed from the IGE model

292 (Pimienta & Duval, 1987; Barnola et al., 1991; Arnaud et al., 2000; Goujon et al., 2003) by implementing a

293 dependency of the firn densification rate on temperature and impurities. The temperature dependence is added on

294 the classical formulation of the densification rate following an Arrhenius law with an activation energy Q as per

295 $\exp(-Q/RT)$ with R the perfect gas constant and T the firn temperature. Rather than using a constant activation

296 energy (Goujon et al., 2003), Bréant et al. (2017) stated that the value of the activation energy should be contingent

297 on the firn temperature value as observed in material science where the temperature dependency exhibits the

298 predominance of one physical mechanism among others for a material compaction at specific temperature.

299 Through several sensitivity tests, Bréant et al. (2017) adjusted three values for activation energy on three different

300 temperature ranges to reproduce best the δ^{15}N evolution over the last deglaciation at East Antarctic sites. The firn

301 model also considers that firn densification is facilitated by the dissolution of impurities within the snow (Freitag

302 et al., 2013). If the impurity content in snow (i.e. concentration of calcium ions) is superior to a certain threshold,

303 the densification rate dependence on impurities is traduced by a relationship between the new activation energy

304 Q' and the concentration of calcium ions $[Ca^{2+}]$: $Q' = f_1 \times (1 - \beta \ln\left(\frac{[Ca^{2+}]}{[Ca^{2+}]_{threshold}}\right)) \times Q$ (Freitag et al., 2013).

305 Bréant et al. (2017) assumed the impurity effect equal for all physical mechanisms and tuned β and f_1 constants

306 so that the modeled-δ^{15}N data mismatch is minimized over the last glacial termination at cold East Antarctic sites.

As a consequence, and in addition to our new extensive δ^{15}N dataset, we have chosen to use here the firn model approach of Bréant et al. (2017). In order to make a correct calculation of uncertainties linked to firn modeling at EDC, we ran two tests of the model with and without including the impurity concentration parameter (see Sect. 3.1 in the Supplementary Material).

The firn densification model takes as input scenarios of temperature and accumulation rate at the surface. It computes both the LID and the thermal gradient in the firn (ΔT), and then deduces the $\delta^{15}N_{therm} = \Omega \cdot \Delta T$ with Ω the thermal fractionation coefficient (Grachev and Severinghaus, 2003). The final δ^{15}N is calculated as $\delta^{15}N = \delta^{15}N_{therm} + \delta^{15}N_{grav}$ and $\delta^{15}N_{grav} \simeq LID \cdot \frac{g}{RT}$ (first order approximation) with g the gravitational acceleration (9.8 m s^{-2}), R the gas constant (8.314 J mol^{-1} K^{-1}) and T the mean firn temperature (K).

3 Age constraints and background scenarios

3.1 ^{81}Kr age constraints

Three ice samples from the bottom part of EDC have been analyzed and provide three age estimates displayed in Table 3: 629, 788 and 887 ka BP with statistical age uncertainties between 30 and 50 kyr, and a 4.8 % systematic error due to the uncertainty in the half-life of ^{81}Kr. The deepest sample suggests the presence of ice older than 800 ka BP below the 3200 m depth level and further studies would be valuable in exploring whether the stratigraphy of EDC lowermost section is continuous (Tison et al., 2015), although this is beyond the scope of this work.

Table 3. Ice samples details and radio krypton dating results. Reported errors are 1σ errors. Upper limits have a 90 % confidence level. The average ^{85}Kr activity in the northern hemisphere is about 75 dpm/cc in 2017. The measured ^{85}Kr concentrations are inferior to the detection limit, verifying that no relevant contamination with modern air has occurred. In addition to the statistical error on the ^{81}Kr age from atom counting, a systematic error due to the uncertainty in the half-life of ^{81}Kr is considered. This error would shift the calculated ^{81}Kr ages up or down for all ice samples. ^{a}dpm/cc = decays per minute per cubic centimeter STP of krypton (conversion: 100 dpm/cc corresponds to ^{85}Kr/Kr = 3.03×10^{11}). ^{b}pMKr = percent Modern Krypton (Jiang et al., 2023).

Depth (m)	Air extracted / Ice weight (mL kg^{-1})	Sample Used (µL STP, Kr)	Analysis Date	^{85}Kr (dpm/cc)^a	^{81}Kr (pMKr)^b	^{81}Kr – age (ka BP) age$^{+stat+sys}_{-stat-sys}$
3013-3024	440/6.0	~0.46	18 Dec 2019	< 0.77	$15.1^{+1.4}_{-1.4}$	629^{+34+31}_{-29-31}
3144-3161	600/8.4	~0.67	30 Dec 2019	< 0.67	$9.6^{+1.0}_{-1.0}$	788^{+36+38}_{-33-38}
3216-3225	415/6.4	~0.43	16 Jan 2020	< 1.17	$7.1^{+1.0}_{-1.0}$	887^{+51+43}_{-44-43}

3.2 Determination of orbital age constraints using new data

3.2.1 $\delta O_2/N_2$

In this work, new highly resolved $\delta O_2/N_2$ data on EDC ice core are presented over Terminations II, III, IV, V and VI (Fig. 1). As these novel $\delta O_2/N_2$ measurements have been performed on ice samples stored at -50°C, there is little storage effect and they can directly be merged with the 800 kyr long record of Extier et al. (2018c) (Table 1). The new dataset improves the resolution of the long EDC record, reaching sub-millennial scale accuracy over MIS 5, 7, 9 and in particular over MIS 11 and MIS 13, periods of sparsity in the ancient record (Extier et al., 2018c). Although the two datasets agree well over recent periods (last 350 kyr), they show some discrepancies during older

periods (between 550 and 375 ka BP, see Fig. 1). Such dissimilarities are observed over MIS 11 (between 424 and 374 ka BP) where the sampling resolution of the previous dataset is particularly low (2,500 years). In addition, the MIS 11 is a period characterized by a low eccentricity in the Earth orbit, inducing subdued variations of insolation, causing $\delta O_2/N_2$ changes of smaller magnitude and leading to lower signal to noise ratio. Data by Landais et al. (2012) (shown by purple squares on Fig. 1 and S2) are consistent with the highly resolved data presented here, supporting the relevance of the new dataset over this period. Over Termination VI (from 550 to 510 ka BP), the old dataset continuously increases while the novel dataset shows a brief maximum at around 525 ka BP followed by a minimum at around 520 ka BP. These newly revealed variations seem in phase with insolation variations, suggesting that the new dataset shows an improved agreement with insolation. Still, highly resolved measurements are needed in the lowermost part of the ice core where noise is significantly altering the temporal signal.

Following a data processing treatment consistent with the method described in Kawamura et al. (2007), the compiled dataset is linearly interpolated every 100 years, and then smoothed using a finite-duration impulse response (FIR) filter with a KaiserBessel20 window (cut-off from 16.7 to 10.0 kyr period, number of coefficients of 559 for the 800 kyr long record) designed with the software Igor Pro, in order to reject periods inferior to 10,000 years and erase the noise present in the data. Note that using a low-pass (rejecting periods below 15 kyr) or a band-pass filter (keeping periods between 100 and 15 kyr periods, used by Bazin et al., 2013) does not alter the peak positions in the $\delta O_2/N_2$ curve (see supplementary Fig. S2). The noise is particularly significant for highly resolved $\delta O_2/N_2$ data and without preliminary filtering, it becomes ambiguous to identify the exact peak position (which needs to be subjectively placed on a 1,000 to 2,000 years interval, see Sect. 2.1 in the Supplementary Material).

The filter is then applied to the local summer solstice insolation curve to check that it does not induce the shift of extrema positions by more than 100 years. This condition is verified over the last 800 kyr, except for the peaks located at the endpoints of the record (respectively around 107 and 788 ka BP) which are then not used for tie points determination. Outliers in the raw $\delta O_2/N_2$ dataset are discarded if they show an anomaly greater than 3.2 ‰ when compared to the low-pass filtered signal. Five outliers are rejected out of 294 points. The $\delta O_2/N_2$ is interpolated and filtered again after removal of the outliers.

The orbital target chosen is the 21st December insolation at 75° South, which is calculated every 100 years over the last 800 kyr (Laskar et al., 2004). The peak positions in the filtered $\delta O_2/N_2$ compiled signal and in the summer solstice insolation are detected via an automated method using the zero values of the time derivatives of the $\delta O_2/N_2$ and its orbital target. Each $\delta O_2/N_2$ maximum is matched to an insolation minimum and each $\delta O_2/N_2$ minimum to an insolation maximum. The data treatment and tie point identification method used here are consistent with the approach recently conducted by Oyabu et al. (2022) on a novel 207 kyr long $\delta O_2/N_2$ record of DF ice core.

Some periods, such as between 450 and 350 ka BP (encompassing MIS 11) and older ages (before 600 ka BP), are characterized by a poor resemblance between the signal and the target. For instance, two or three peaks in the insolation curve only correspond respectively to one or two peaks in the $\delta O_2/N_2$ data. This could be explained by a low eccentricity-induced subdued variability in the insolation target and hence in $\delta O_2/N_2$ signal over MIS 11 and to the poor resolution of the $\delta O_2/N_2$ measurements before 600 ka BP. In such cases, the uncertainty (1σ) associated with each tie point is ranging from 6 to 10 kyr (precession half period) and some extrema in the target are not used to tune the $\delta O_2/N_2$ record (5 extrema over MIS 11 out of 63 over the last 800 kyr). Otherwise, $\delta O_2/N_2$ seems to evolve in phase with the inverse summer solstice insolation variations and the tie points uncertainty (1σ)

is set at 3 kyr. A 3-4 kyr uncertainty was evaluated by Bazin et al. (2016) on the following arguments. They examined three $\delta O_2/N_2$ records from Vostok, Dome Fuji and EDC ice cores over MIS 5 and detected some site-specific $\delta O_2/N_2$ high frequency variability that could not be explained by a timescale issue. This observation, along with the presence of a 100 kyr periodicity in the EDC $\delta O_2/N_2$ record and the difficulty of identifying $\delta O_2/N_2$ mid-slopes and maxima because of a scattering of the $\delta O_2/N_2$ signal at millennial scale, led them to recommend the use of a 3-4 kyr uncertainty. Because our higher resolution $\delta O_2/N_2$ data gives the possibility to filter the signal with more confidence and hence reduces the uncertainty in the identification of $\delta O_2/N_2$ tie points, we propose to take a 3-kyr uncertainty. The orbital tuning results in 58 new tie points over the last 800 kyr (displayed in Fig. 1 and compiled in supplementary Table S5), replacing the 20 tie points used to constrain AICC2012 between 800 and 300 ka BP that were derived from synchronizing mid-slopes of band-pass filtered $\delta O_2/N_2$ with the insolation (Bazin et al., 2013).
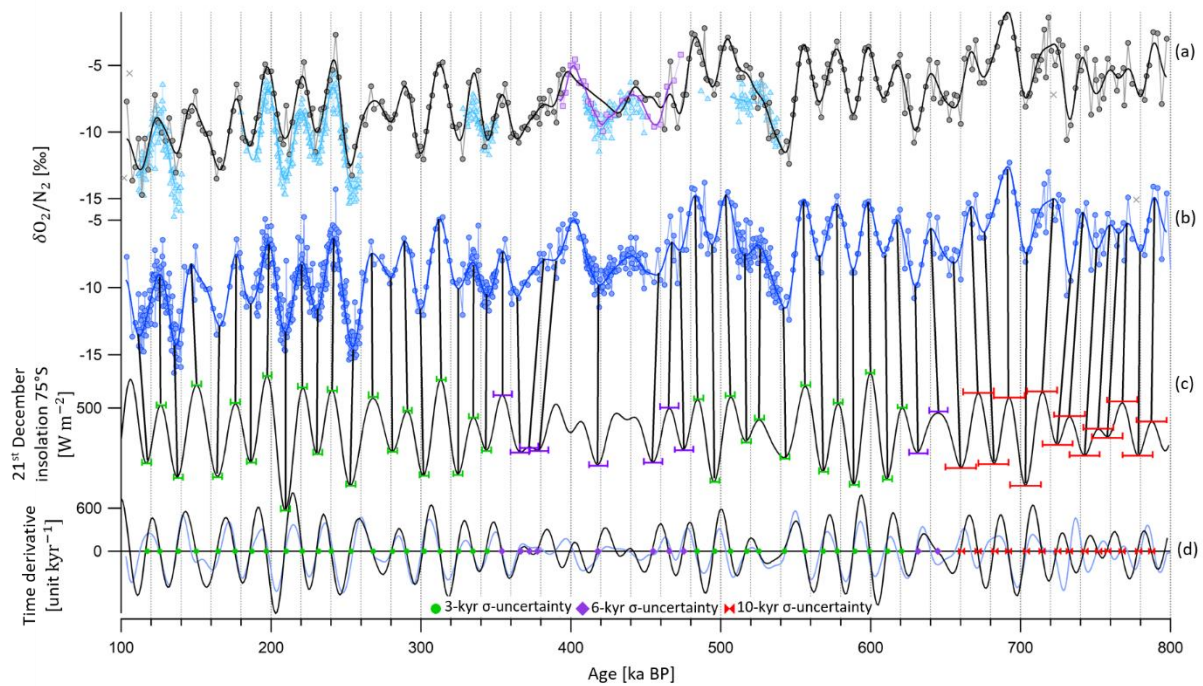
Figure 1. Alignment of $\delta O_2/N_2$ and insolation between 800 and 100 ka BP. (a) EDC raw $\delta O_2/N_2$ old data between 800 and 100 ka BP (black circles for data of Extier et al., 2018c; and purple squares for data of Landais et al., 2012), outliers (grey crosses) and filtered signal (black and purple lines). EDC raw $\delta O_2/N_2$ new data (blue triangles, this study) and filtered signals (blue line). The $\delta O_2/N_2$ data are plotted on AICC2012 ice timescale. Zooms between 270 and 100 ka BP and between 570 and 300 ka BP are shown in supplementary Fig. S2. (b) Extrema in the compiled filtered $\delta O_2/N_2$ dataset (blue plain line) are identified and matched to extrema in the (c) 21st December insolation at 75° South plotted on a reversed y-axis and on the age scale given by Laskar et al. (2004) (black line). The peaks are matched by black vertical bars. (d) The 0 value in the time derivative of insolation (black line) and of the filtered $\delta O_2/N_2$ dataset (blue line) corresponds to extreme values in the signals. The determined tie points between $\delta O_2/N_2$ and insolation are depicted by markers on the horizontal line. Green circles are attached to a 3 kyr 1σ-uncertainty (green horizontal error-bars show 2σ in panel c), purples squares are associated with a 6 kyr 1σ-uncertainty (purple horizontal error-bars show 2σ in panel c) and red markers with a 10 kyr 1σ-uncertainty (red horizontal error-bars show 2σ in panel c). Between 390 and 475 ka BP, all extrema are not tuned to the target due to the poor resemblance between the signal and insolation.

The uncertainty arising from the filter used and from the tie point identification method can be estimated by a comparison of the $\delta O_2/N_2$ peak positions identified before and after filtering of the signal with two different

methods (see Sect. 2.1 in the Supplementary Material). The resulting uncertainty is of 700 years on average (with a standard deviation of 250 years), reaching 2,100 years around 230 ka BP.

The new highly resolved data presented here enable a better description of the signal variability and a reduction of the uncertainty associated with orbital tie points.

3.2.2 Total Air Content

The TAC record is extended over the last 800 kyr with a mean sampling resolution of 2,000 years (Fig. 2). The raw data between 800 and 440 ka BP are not shown here and will be published in a separate study (Capron et al., in prep). The TAC series shows a good resemblance with the integrated summer insolation (ISI, obtained by a summation over a year of all daily insolation at 75° South above a chosen threshold). After comparing the EDC TAC record, within its frequency domain, with ISI curves obtained using different thresholds, the ISI curve calculated for a threshold of 375 W m^{-2} (ISI375) exhibits the finest spectral agreement with the EDC TAC record over the past 800 kyr. The coherency between the TAC record and ISI is deficient over MIS 11 (between 430 and 370 ka BP) and in the deepest part of the core (prior to 700 ka BP) where the signal to noise ratio is low.

Following a data processing treatment consistent with the method described by Lipenkov et al. (2011), the 800 kyr long TAC dataset is interpolated every 100 years, and then filtered with a band-pass filter rejecting periods below 15,000 and above 46,000 years (IgorPro FIR filter with a KaiserBessel20 window: cut-off from 15 to 14 kyr period and from 46 to 47 kyr period, number of coefficients of 559). Outliers in the raw TAC dataset are discarded if they show an anomaly superior to 1.0 mL kg^{-1} (standard deviation of TAC record) when compared to the band-pass filtered signal. 45 outliers are rejected out of 399 datapoints (among which 16 outliers are identified between 100 and 0 ka BP). The TAC is interpolated and filtered again after removal of the outliers.

Tie points are mostly determined by matching variations extrema of TAC and integrated summer insolation at 75°S (Fig. 2). Indeed, in case of a non-linear relationship between TAC and insolation, extrema are better indicators of TAC response to insolation forcing. Moreover, filtering the dataset induces a bias in the mid-slope position. The method employed to determine extrema position is the same as for $\delta O_2/N_2$ insolation tie points. Only one of the tie points is identified by matching mid-slopes (i.e. derivative extremum) at 362 ka BP rather than minima at 375 ka BP due to the flatness of the insolation minimum which precludes to identify an accurate tie point. Not all extrema are tuned to the target due to the poor resemblance between the signal and insolation and 42 unambiguous tie points were kept out of 64 detected by the automated method. The tie point uncertainty finds its origin in the age errors associated with the filtering (~700 years), tie point identification and outlier rejection (~900 years). The 1σ-uncertainty is evaluated to be 3 kyr when there are good agreements: (i) between the signal and its target, meaning that one peak in ISI375 is reflected by a singular peak in the TAC record, and (ii) between the tie points identified by the automated method and manually (age shift < 1,300 years, average value) (see green circles, Fig. 2). A 6 kyr uncertainty (1σ) is attached to the tie points if the latter condition is not respected (age shift > 1,300 years) (see purple squares, Fig. 2) and a 10 kyr uncertainty (1σ) (precession half period) is inferred to the tie points if the ISI375 variations are not reflected by the TAC record, meaning that one peak in ISI375 could be associated with two peaks in the TAC record, or if the signal to noise ratio of the TAC record is too large (see red markers, Fig. 2). The choices of filter and orbital target have no significant impact on the chronological uncertainty, a further detailed study is thus beyond the scope of this work.
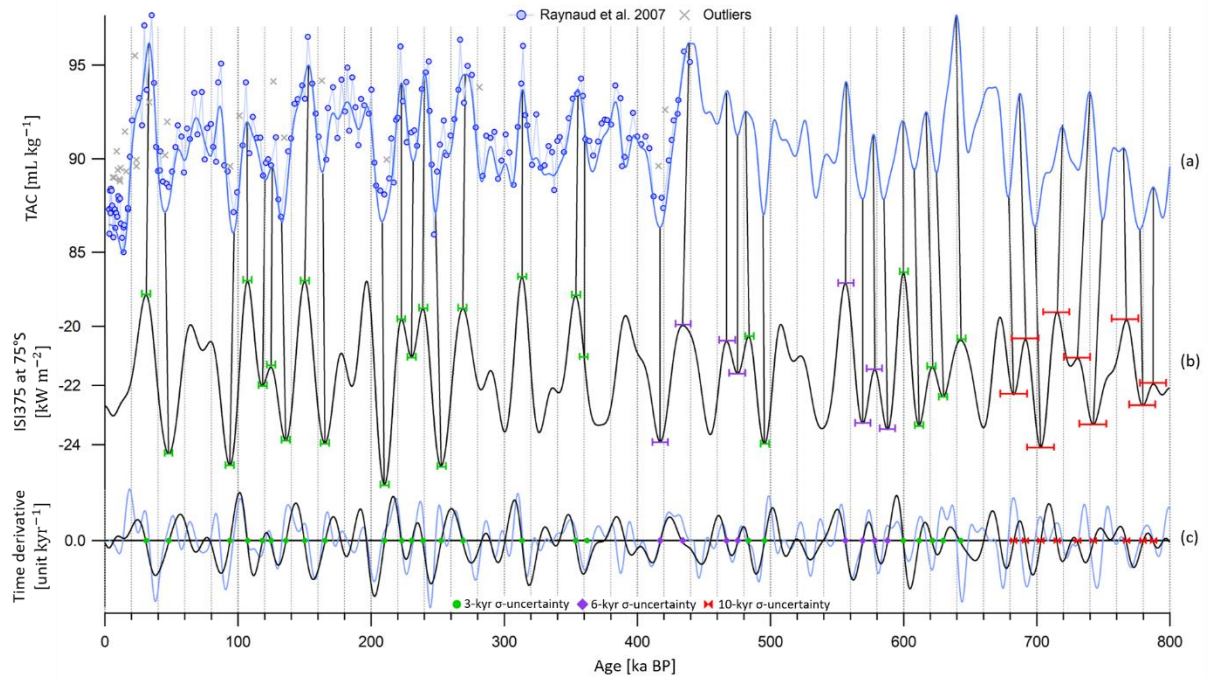
Figure 2. Alignment of TAC and insolation between 800 and 0 ka BP. (a) EDC raw TAC data (blue circles, Raynaud et al., 2007), outliers (grey crosses) and filtered signal (blue line) on AICC2012 ice timescale. The raw data between 800 and 440 ka BP are not shown here and will be published in a separate study (Capron et al., in prep). (b) ISI375 at 75°S on a reversed axis. The peaks and mid-slopes are matched by vertical bars. (c) Temporal derivative of insolation (black line) and TAC (blue line). Its 0 value corresponds to extreme values in insolation and TAC. The determined tie points between TAC and insolation are depicted by markers on the horizontal line. Green circles are attached to a 3 kyr 1σ-uncertainty (green horizontal error-bars show 2σ in panel c), purples squares are associated with a 6 kyr 1σ-uncertainty (purple horizontal error-bars show 2σ in panel c) and red markers with a 10 kyr 1σ-uncertainty (red horizontal error-bars show 2σ in panel c).

The orbital tuning results in 42 new tie points over the last 800 kyr (displayed in Fig. 2 and compiled in Table S5). They replace the 14 tie points used to constrain EDC ice timescale in AICC2012 between 425 and 0 ka BP, that were derived by direct matching mid-slope variations of unfiltered TAC and ISI target and attached to an uncertainty varying between 2.9 and 7.2 kyr.

3.2.3 $\delta^{18}O_{atm}$

In this work, new highly resolved $\delta^{18}O_{atm}$ data on EDC ice core are presented over Terminations II, III, IV, V and VI (Fig. 3). The available $\delta^{18}O_{atm}$ data can be sorted out in two groups: new $\delta^{18}O_{atm}$ data (Grisart, 2023) at high temporal resolution (between 333 and 1,375 years, see Table 1) and old measurements compiled by Extier et al. (2018b), characterised by a lower sampling resolution (between 1,000 and 1,500 years, see Table 1), except between 374 and 153 ka BP (resolution between 160 and 700 years, see Table 1). The new dataset improves the resolution of the long EDC record over MIS 5, 7, 9 and in particular over MIS 11 and 13, periods of sparsity in the ancient record (Extier et al., 2018b). Although the two datasets agree globally well over the last 800 kyr, the new highly resolved dataset refines the signal between 255.5 and 243 ka BP where a lot of noise is present in the record of Extier et al. (2018b) (see inset in Fig. 3). This noise may be explained by the fact that highly resolved (mean sampling resolution of 381 years) measurements were performed on ice samples stored at -20°C in the compilation by Extier et al. (2018b) while the new measurements are performed on ice stored at -50°C. Therefore,

we chose to remove the noisy dataset of Extier et al. (2018b) between 255.5 and 243 ka BP before combining the novel dataset with the remaining 800 kyr long record of Extier et al. (2018b).
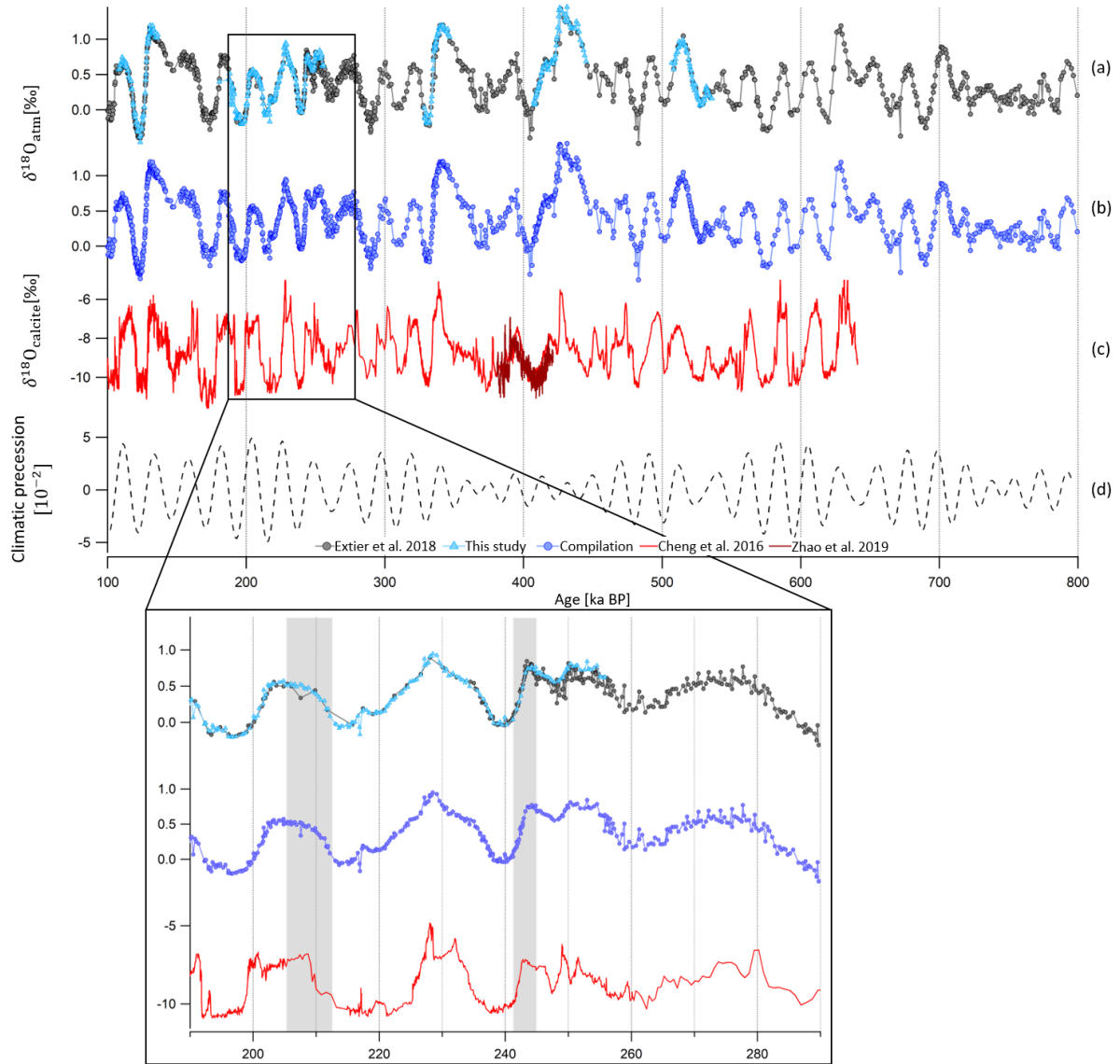

Figure 3. Evolution of EDC $\delta^{18}O_{atm}$ record between 800 and 100 ka BP. (a) EDC $\delta^{18}O_{atm}$ raw old data (black circles, Extier et al., 2018b) and EDC $\delta^{18}O_{atm}$ raw new data (blue triangles, Grisart, 2023) on AICC2012 gas timescale. (b) Compilation of the two datasets after removal of old measurements between 255.5 and 243 ka BP. (c) $\delta^{18}O_{calcite}$ composite record from speleothems from Sambao, Dongge, Hulu (red line) and Yongxing (brown line) caves (Cheng et al., 2016; Zhao et al., 2019) on U-Th age scales. (d) Climatic precession from Laskar et al. (2004) delayed by 5,000 years. Inset is a zoom between 290 and 190 ka BP. Grey vertical squares highlight the improved agreement between new data of Grisart (2023) (blue triangles) and $\delta^{18}O_{calcite}$ (red line) than between old data (grey circles) and $\delta^{18}O_{calcite}$.

Following the dating approach proposed by Extier et al. (2018a), $\delta^{18}O_{atm}$ and $\delta^{18}O_{calcite}$ are aligned using mid-slopes of their variations over the last 640 kyr. To do so, the compiled EDC $\delta^{18}O_{atm}$ record and the Chinese $\delta^{18}O_{calcite}$ signal are linearly interpolated every 100 years, smoothed (25 points Savitzky-Golay) and extrema in their temporal derivative are aligned. It should be specified that synchronizing $\delta^{18}O_{atm}$ and East Asian $\delta^{18}O_{calcite}$ is not always obvious due to the long residence time of oxygen in the atmosphere (1-2 kyr) which may not be compatible with $\delta^{18}O_{calcite}$ abrupt variations over glacial inceptions and terminations. In particular, the slow increase of the

484    $\delta^{18}O_{atm}$ record from 370 to 340 ka BP does not resemble the evolution of $\delta^{18}O_{calcite}$ which is first moderate then

485   abrupt over the same period (Fig. 4, red area). For this reason, we chose not to use the two tie points identified by

486   Extier et al. (2018a) at 351 and 370.6 ka BP. The new highly resolved data enable to identify five new tie points

487   and to shift five tie points that have been determined beforehand by Extier et al. (2018a) (Fig. 4). Between 248

488   and 244 ka BP, the new $\delta^{18}O_{atm}$ measurements do not coincide with the $\delta^{18}O_{calcite}$ variations and we decided to

489   remove the tie point identified by Extier et al. (2018a) at 245.4 ka BP (Fig. 4, red area). Between 480 and 447 ka

490   BP, the $\delta^{18}O_{atm}$ variations are characterized by a low resolution (1.1 kyr) and a weak amplitude, which prevents

491   unambiguous matching of $\delta^{18}O_{atm}$ and $\delta^{18}O_{calcite}$. The four tie points identified by Extier et al. (2018a) at 447.3,

492   449.9, 455.9 and 462.8 ka BP are thus rejected (Fig. 4, red area). The remaining 39 tie points defined by Extier et

493   al. (2018a) are preserved and used here to constrain EDC gas age. Their uncertainty (1σ) varies between 1.1 and

494   7.4 kyr.
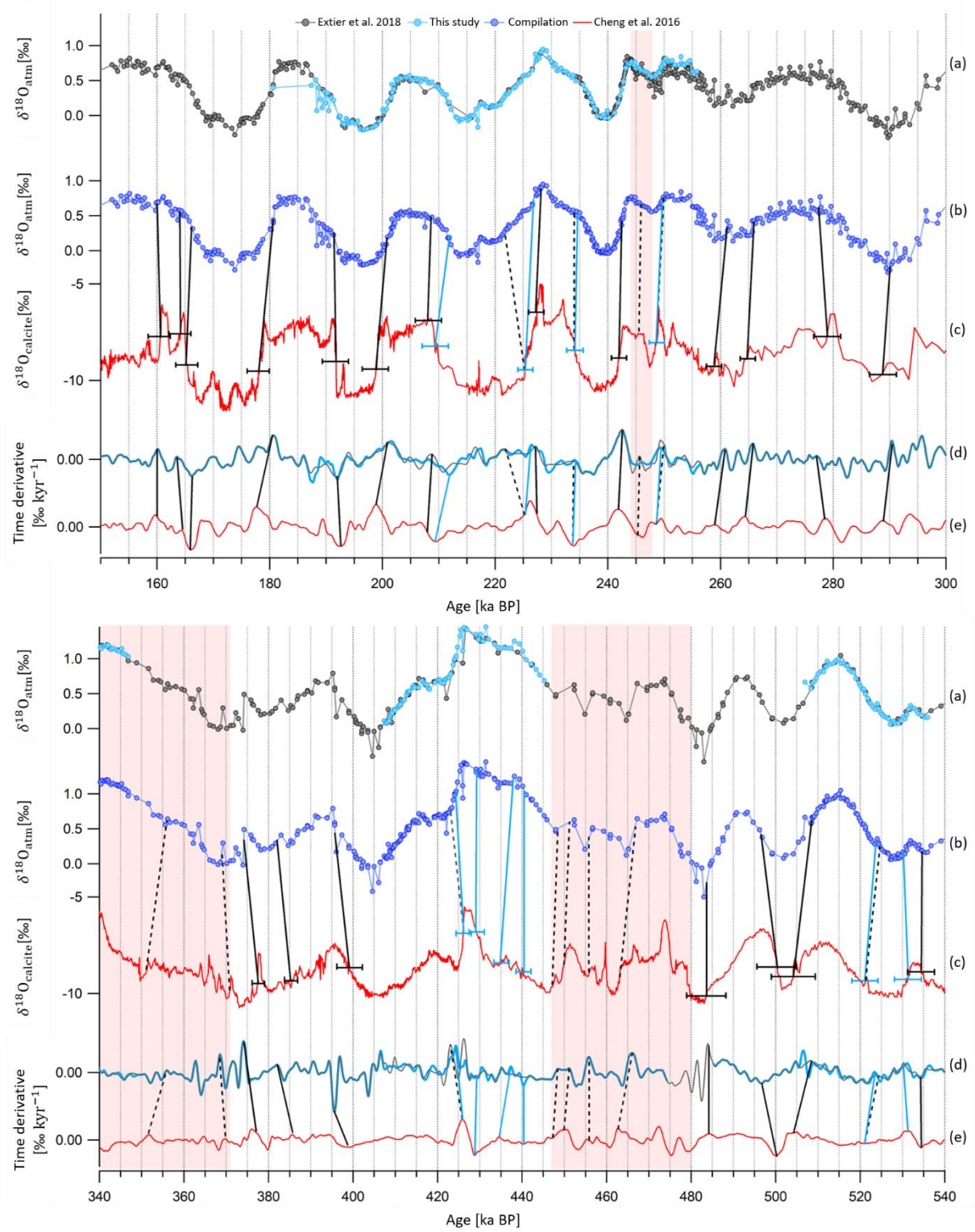
Figure 4. Alignment of EDC $\delta^{18}O_{atm}$ and Chinese $\delta^{18}O_{calcite}$ records over time periods where new tie points are defined. (a) EDC $\delta^{18}O_{atm}$ new and old datasets on AICC2012 gas age scale. (b) Compiled EDC $\delta^{18}O_{atm}$. (c) Chinese $\delta^{18}O_{calcite}$ on U-Th age scale (Cheng et al., 2016). (d) Temporal derivatives of compiled EDC $\delta^{18}O_{atm}$ (blue curve) and of the old $\delta^{18}O_{atm}$ dataset (black curve). (e) Temporal derivative of Chinese $\delta^{18}O_{calcite}$ (red curve). Extrema in temporal derivatives are matched. Tie points represented by black vertical bars are determined by Extier et al. (2018a) and those by blue vertical bars are determined by this study. Both are used in the AICC2023 chronology. Dashed vertical bars show tie points identified by Extier et al. (2018a) that are not used in AICC2023. 2σ uncertainties attached to the tie points are shown by the horizontal error-bars in panel c). Red vertical areas frame periods of lacking resemblance between $\delta^{18}O_{atm}$ and $\delta^{18}O_{calcite}$ variations.

17

503   Between 810 and 590 ka BP, the $\delta^{18}O_{atm}$-$\delta^{18}O_{calcite}$ dating uncertainty becomes larger than 6 kyr and no

504   East Asian speleothem $\delta^{18}O_{calcite}$ records are available before 640 ka BP. Over this time interval, we updated the

505   following approach of Bazin et al. (2013): EDC $\delta^{18}O_{atm}$ and 5 kyr delayed climatic precession are synchronized

506   using mid-slopes of their variations. However, from the findings of Extier et al. (2018a), $\delta^{18}O_{atm}$ should rather be

507   aligned to precession without delay when no Heinrich-like events occurs. Indeed, $\delta^{18}O_{atm}$ is sensitive to both orbital

508   and millennial scale variations of the low latitude water cycle (Landais et al., 2010; Capron et al., 2012) and

509   Heinrich-like events occurring during deglaciations delay the response of $\delta^{18}O_{atm}$ to orbital forcing through

510   southward ITCZ shifts (Extier et al., 2018a). We thus chose to align $\delta^{18}O_{atm}$ to precession when no Ice Rafted

511   Debris (IRD) peak is visible on the studied period in the ODP983 record (Barker, 2021) and keep a 5 kyr delay

512   when IRD peaks are identified. This results in shifting 12 tie points of Bazin et al. (2013) by 5,000 years towards

513   older ages (Fig. 6). The eight remaining tie points of Bazin et al. (2013) that coincide with peaks in the IRD record

514   are kept (Fig. 6). To confirm the validity of our approach, we tested three methodologies to align $\delta^{18}O_{atm}$ and

515   precession over well-dated periods when $\delta^{18}O_{atm}$-$\delta^{18}O_{calcite}$ matching was done (see Sect. 2.2.2 in the

516   Supplementary Material). These tests support our approach but in order to account for potential errors associated

517   with this tuning method (Oyabu et al., 2022), a 6 kyr uncertainty (1σ) is attributed to the $\delta^{18}O_{atm}$ derived tie points

518   over the period between 810 and 590 ka BP.

519   69 new $\delta^{18}O_{atm}$ tie points are determined over the last 810 kyr (displayed in Fig. 4 and 5 and compiled in

520   Table S5). They replace the 39 tie points used to constrain EDC gas timescale in AICC2012 between 800 and 363

521   ka BP (Bazin et al., 2013). The age constraints are attached to an uncertainty varying between 1.1 and 7.4 kyr

522   which is the sum of the uncertainties of the speleothems ^{230}Th dating, the $\delta^{18}O_{atm}$ response to orbital forcing (1

523   kyr) and the $\delta^{18}O_{atm}$ - $\delta^{18}O_{calcite}$ matching (0.5 kyr). The same alignment method is applied between Vostok $\delta^{18}O_{atm}$

524   (Petit et al., 1999) and Chinese $\delta^{18}O_{calcite}$ and 36 new tie points are determined (see Sect. 4.1.2 in the Supplementary

525   Material), replacing the 35 tie points used to constrain Vostok gas timescale in AICC2012.

526   Finally, there was a redundancy in the dating of the bottom part of the EDC ice core in AICC2012 where

527   both $\delta^{18}O_{atm}$ orbital tie points and ^{10}Be peaks corresponding to the Matuyama-Brunhes geomagnetic reversal event

528   were used. Indeed, the two ^{10}Be dating constraints at 780.3 and 798.3 ka BP were directly derived from the $\delta^{18}O_{atm}$

529   orbital dating and not obtained independently (Dreyfus et al., 2008). We thus decide to remove the ^{10}Be age

530   constraints.
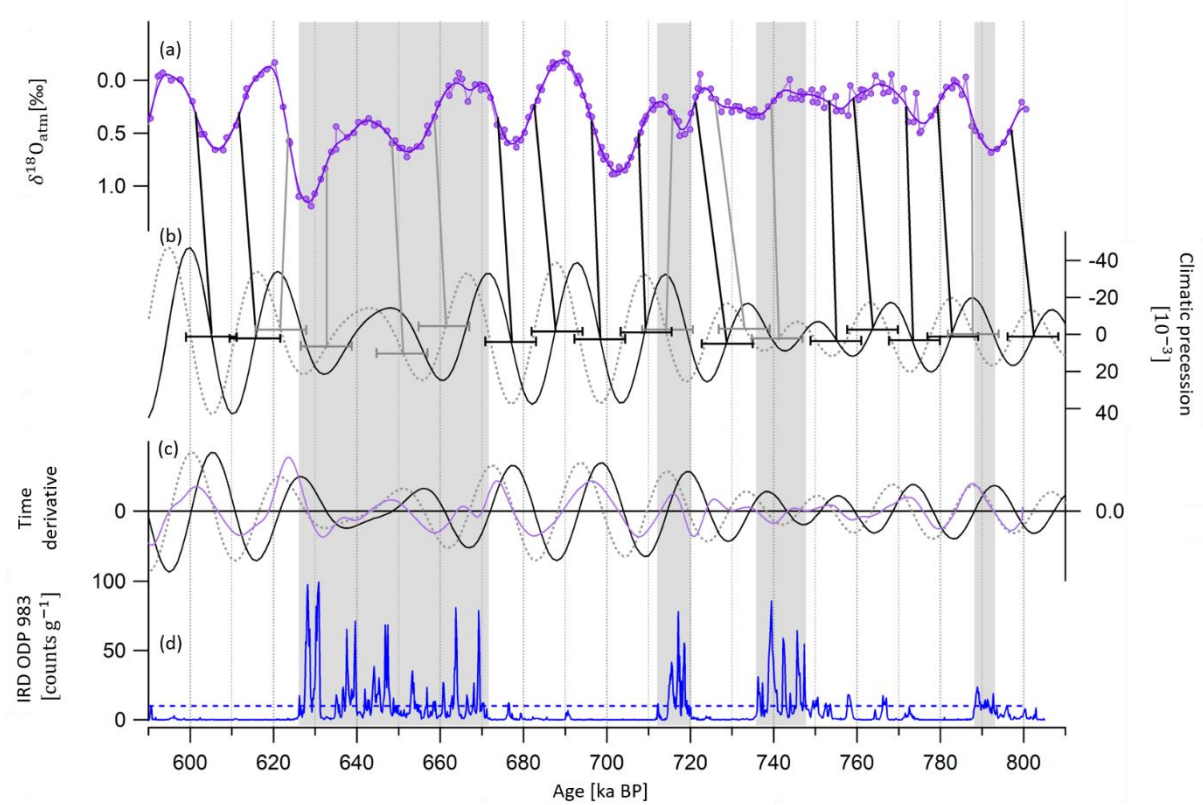
Figure 5. Alignment of EDC $\delta^{18}O_{atm}$ and climatic precession between 810 and 590 ka BP. (a) Compiled EDC $\delta^{18}O_{atm}$ on AICC2012 gas timescale. (b) Precession delayed by 5,000 years (grey dashed line) and not delayed (black line) (Laskar et al., 2004). (c) Temporal derivative of precession (black line), delayed precession (grey dotted line) and of the compiled $\delta^{18}O_{atm}$ record (purple plain line). (d) Ice-Rafted Debris at ODP983 site (North Atlantic Ocean, southwest of Iceland) by Barker (2021). The gray squares indicate periods where IRD counts are superior to the 10 counts g^{-1} threshold shown by the blue dotted horizontal line. Grey vertical bars illustrate new tie points between EDC $\delta^{18}O_{atm}$ and delayed precession mid-slopes (i.e. derivative extrema) when IRD counts are superior to the threshold. Black vertical bars illustrate new tie points between EDC $\delta^{18}O_{atm}$ and precession mid-slopes (i.e. derivative extrema) when no Heinrich-like events is shown by IRD record. The 12 kyr 2σ-uncertainty attached to the tie points is shown by the horizontal error-bars in panel b.

3.3 Background scenario of LID

In this work, new highly resolved data $\delta^{15}N$ on EDC ice core are presented over Terminations II, III, IV, V and VI (Fig. 6a). The available $\delta^{15}N$ data can be sorted out in two groups: $\delta^{15}N$ measured by Grisart (2023) and Bréant et al. (2019) at high temporal resolution (between 333 and 1,375 years, see Table 1) and the older measurements (Bazin et al., 2013) used to estimate LID in AICC2012, characterized by a lower sampling resolution (between 1,400 and 2,400 years, see Table 1). The measurements of Bazin et al. (2013) and Bréant et al. (2019) have been shifted down by 0.04 ‰ to account for calibration errors. The new dataset permits to extend the record around 1100 m and between 1700 and 2500 m and to improve the resolution over Terminations II to VI.
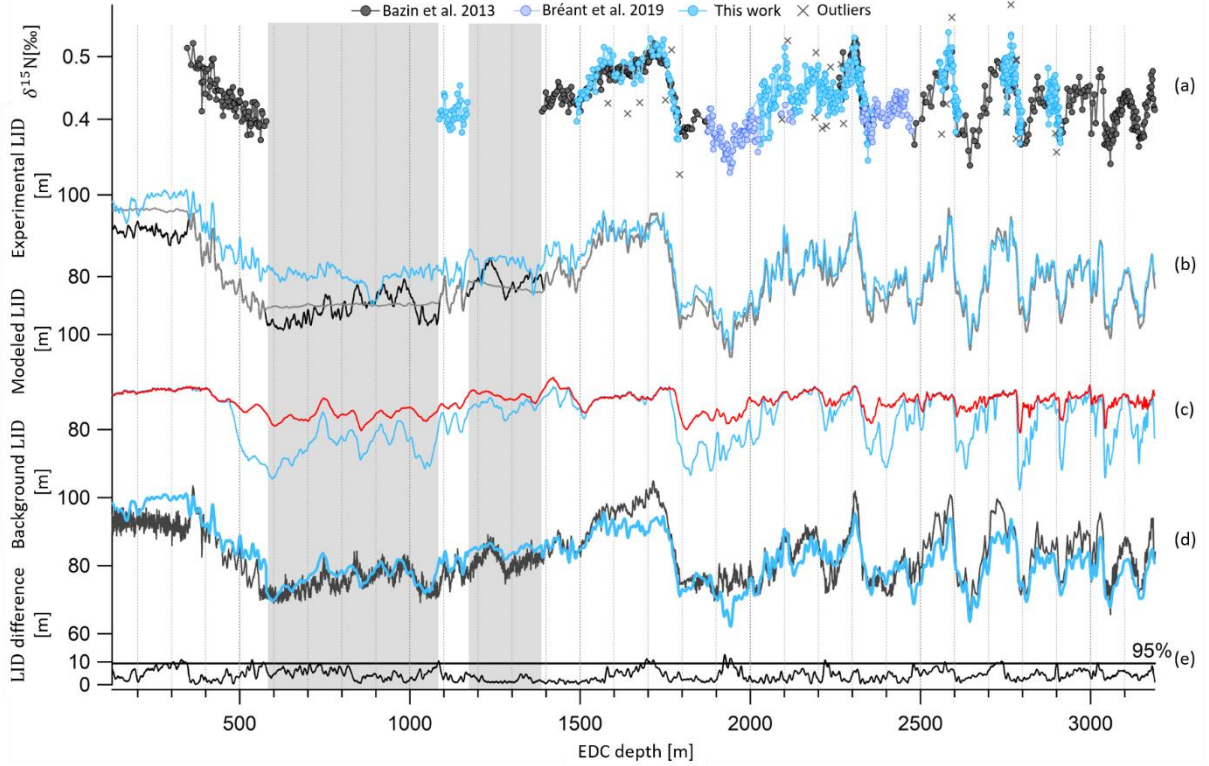
Figure 6. EDC δ^{15}N record and past LID evolution as a function of EDC depth. (a) New and highly-resolved δ^{15}N dataset (blue circles), dataset of Bréant et al. (2019) (purple circles), old dataset (black circles) and outliers (rejection criterion of 1σ) (grey crosses). (b) LID calculated as per LID $\simeq \delta^{15}$N$_{grav} \cdot \frac{RT}{g}$ for three cases: (1) δ^{15}N$_{grav} = \delta^{15}$N with the δ^{15}N record constructed by interpolation between data when no data are available (grey), (2) δ^{15}N$_{grav} = \delta^{15}$N with the δ^{15}N record constructed by normalization of the δD record when no data are available (black), (3) δ^{15}N$_{grav} = \delta^{15}$N - δ^{15}N$_{therm}$ with δ^{15}N$_{therm}$ estimated by the firn model (Bréant et al., 2017) and the δ^{15}N record constructed by interpolation between data when no data are available (blue). (c) Modeled LID with impurity concentration (blue) and without impurity concentration (red). (d) Background scenarios of LID used to construct AICC2012 (black) and inputs in Paleochrono to obtain AICC2023 (blue). (e) Absolute difference between prior LID of AICC2012 and AICC2023. The grey line separates the 5 % highest values from the rest. The grey rectangles cover areas when no δ^{15}N data are available.

Outliers are discarded if they show an anomaly superior to 0.045 ‰ when compared to the smoothed record (Savitzky-Golay algorithm with 25 points). This results in the rejection of 25 datapoints out of 475 measurements for the new dataset (Fig. 6). The two δ^{15}N datasets are merged and the compiled record is interpolated every 100 years. Then, assuming that the firn is solely a diffusive zone (i.e. no convection layer at the top) at EDC during the last 800 kyr, in agreement with current observations (Landais et al., 2006), past LID is calculated as per the first order estimate of the barometric equation:

$$LID \simeq \delta^{15}N_{grav} \cdot \frac{RT}{g} \qquad (5)$$

with T the temperature at EDC estimated from combined measurements of ice δ^{18}O and δD after correction of the influence of the sea water δ^{18}O (Landais et al., 2021).

In absence of a large thermal gradient within the firn (mostly present in Greenlandic ice cores during Dansgaard Oeschger events), δ^{15}N is mainly modulated by gravitational fractionation of N$_2$ molecules occurring from the surface down to the lock-in zone, and δ^{15}N measured in bubbles hence approximately reflects the LID

20

573 (Severinghaus et al., 1996; Landais et al., 2006) and $\delta^{15}N_{grav} \simeq \delta^{15}N$ in Eq. (5) (grey and black lines in Fig. 6b).

574 To account for a small temperature gradient in the firn in Antarctic ice core, the thermal fractionation term $\delta^{15}N_{therm}$

575 can be estimated by the firn model (Bréant et al., 2017). Past LID is then calculated as per Eq. (5) with $\delta^{15}N_{grav} =$

576 $\delta^{15}N$ - $\delta^{15}N_{therm}$ (blue curve in Fig. 6b). Thermal fractionation represents a maximum correction of 4.2 m on the

577 LID at EDC.

578 When $\delta^{15}N$ measurements are not available, Bazin et al. (2013) used a synthetic $\delta^{15}N$ signal based on the

579 correlation between $\delta^{15}N$ and δD to estimate the LID background scenario at Dome C (black curve in Fig. 6b).

580 Indeed, for different low accumulation Antarctic sites, it has been observed that $\delta^{15}N$ and δD are well correlated

581 over the last Termination on a coherent timescale (Dreyfus et al., 2010; Capron et al., 2013). Since then, Bréant et

582 al. (2019) presented new high resolution EDC measurements of $\delta^{15}N$ extending the signal over Termination III

583 (around 2300 m, 250 ka BP). Their study unveiled the anatomy of this atypical deglaciation: the interplay between

584 Heinrich-like events and bipolar seesaw mechanism induced a strong warming of Antarctic temperature, resulting

585 in divergent $\delta^{15}N$ and δD records. Therefore, using δD to construct a synthetic $\delta^{15}N$ scenario should be done

586 carefully. For this reason, the firn densification model described in Bréant et al. (2017) is employed to estimate

587 EDC LID evolution in the past when $\delta^{15}N$ data are missing, rather than using the $\delta^{15}N$-δD relationship, as it was

588 done for AICC2012. After different sensitivity tests, we choose to keep the parameterization preferred by Bréant

589 et al. (2017) (i.e. firn densification activation energy depending on the temperature and the impurity concentration)

590 as it is believed to give the most probable evolution of LID over the last 800 kyr (see Sect. 3.1 in the Supplementary

591 Material).

592 The final background LID scenario is calculated as a function of EDC depth (Table 4, Fig. 6d). It has

593 been smoothed using a Savitzky-Golay algorithm (25 points), and then provided as an input file to Paleochrono.

594 **Table 4. Method of determination of the background LID scenario according to EDC depth range.**

Depth range (m)	0 – 345	345 - 578	578 - 1086	1086 – 1169	1169 – 1386	1386 – Bottom
$\delta^{15}N$ data availability	No	Yes	No	Yes	No	Yes
Method of determination of the LID	From constant $\delta^{15}N$ (measured at 345 m) and corrected for thermal fractionation.	From $\delta^{15}N$ data, corrected for thermal fractionation and smoothed.	From firn modeling.	From $\delta^{15}N$ data, corrected for thermal fractionation and smoothed.	From firn modeling.	From $\delta^{15}N$ data, corrected for thermal fractionation and smoothed.

595

596 The other necessary input files for Paleochrono, Accumulation (A) and Thinning (τ) background scenarios,

597 are the same as in Bazin et al. (2013). A is estimated from water isotopes (Parrenin et al., 2007b) and τ from

598 unidimensional ice-flow modeling (Parrenin et al., 2007a).

599 **3.4 New stratigraphic links between EDC and other ice cores**

600 EDC can be linked to other ice cores via ice and gas stratigraphic links identified during abrupt climate changes

601 recorded in Greenlandic and Antarctic ice cores. To establish AICC2012, Bazin et al. (2013) used 255 gas

stratigraphic tie points coming from the matching of CH_4 (or $\delta^{15}N$ when CH_4 is not available at NGRIP) or $\delta^{18}O_{atm}$ variations between EDC, EDML, Vostok, NGRIP and TALDICE. Here we revise some of these tie points using the synchronization of CH_4 series of EDC, Vostok and TALDICE to up-to-date highly resolved records from EDML and NGRIP ice cores over the last interglacial offset and the last glacial period (Baumgartner et al., 2014). From 122 to 10 ka BP, Baumgartner et al. (2014) identified 39 stratigraphic links between EDML and NGRIP by matching mid-points of the CH_4 abrupt changes with a precision of 300 to 700 years. When they also detected such rapid variations in lower resolution CH_4 records of TALDICE, Vostok and EDC ice cores, they extended the stratigraphic links to the five ice cores but assigned them a larger uncertainty (up to 1,500 years). AICC2012 was further constrained by 534 ice stratigraphic links identified from volcanic matching and synchronization of cosmogenic isotopes between the five ice cores. Here we replace some of the stratigraphic links between NGRIP, EDML and EDC by highly resolved volcanic matching points (Svensson et al., 2020). The application of volcanic proxies and annual layer counting helped them identify large volcanic eruptions that left a specific signature in both Greenland and Antarctica. Such signature is defined by sulfate patterns (indicating singular volcanic events separated by the same time interval in ice cores from both poles). Their study spotted 82 large bipolar volcanic eruptions over the second half of the last glacial period (from 60 to 12 ka BP), providing as many ice stratigraphic links synchronizing EDC with EDML and EDML with NGRIP within a small relative uncertainty (i.e. ranging from 1 to 50 years, of 12 years on average). Between 43 and 40 ka BP, five cosmogenic tie points associated with the Laschamp geomagnetic excursion (Raisbeck et al., 2017) replace the volcanic matching over this period (Svensson et al., 2013), shifting the tie points by ∼30 years.

4 Discussion

4.1 New AICC2023 chronology

4.1.1 Impact of absolute age constraints

A large uncertainty is linked with ^{81}Kr dating, therefore ^{81}Kr age estimates do not significantly change the chronology (maximum 200 years) (Fig. 7). ^{81}Kr age estimates are systematically older than the new timescale (by 25 to 36 kyr, see Fig. 8). This observation could also indicate an undervaluation of ^{81}Kr half-life.

4.1.2 Consistency between orbital age constraints

To evaluate the consistency between the orbital age constraints, several "test chronologies" are produced. Each "test chronology" of EDC ice core is obtained by running one multi-site (EDC, Vostok, EDML, TALDICE, NGRIP) experiment of Paleochrono. In each of these tests, we implemented one category of new age constraints presented in this work while keeping AICC2012 parameters for other categories. Several "test chronologies" are thus constructed: the ^{81}Kr, $\delta O_2/N_2$, TAC, $\delta^{18}O_{atm}$, CH_4 matching and volcanic matching based chronologies (Fig. 7). Two additional "test chronologies" are obtained by implementing and modifying age constraints either on Vostok or TALDICE with respect to the AICC2012 chronology as explained in Sect. 2.1 (Fig. 7, dotted lines). EDC ice age difference between each "test chronology" and the AICC2012 timescale is represented in Fig. 7 so that it is possible to read which type of dating tool suggests to shift the background chronology towards either older or younger ages.

Although the three orbital dating tools globally agree with each other over the last 800 kyr, meaning that they all tend to shift the background chronology towards either older or younger ages over a certain period of time, they sometimes are inconsistent (Fig. 7). The three largest inconsistencies involve age differences between $\delta O_2/N_2$, TAC and $\delta^{18}O_{atm}$ based chronologies reaching 4.15 to 8.3 kyr (Table 5). At 390 ka BP, an 8.3 kyr large discrepancy is observed between $\delta O_2/N_2$ and $\delta^{18}O_{atm}$ based chronologies. Over this period, the low resolution $\delta O_2/N_2$ record variations do not match its orbital target variations (two insolation minima against one $\delta O_2/N_2$ maximum, see Fig. 1). For this reason, the $\delta O_2/N_2$ age constraints identified between 480 and 350 ka BP were attached to a 6 kyr uncertainty (quarter of a recession period, Fig. 1). In contrast, the $\delta^{18}O_{atm}$ record agrees well with $\delta^{18}O_{calcite}$ (Fig. 3) and the uncertainty attached to the $\delta^{18}O_{calcite}$ inferred tie points over this interval is smaller. Hence, the new AICC2023 chronology suggests to shift AICC2012 towards older ages by 2.2 kyr, as per the $\delta^{18}O_{atm}$ based chronology (Fig. 7). Around 550 ka BP, the TAC and $\delta^{18}O_{atm}$ based chronologies strongly diverge. This may be caused by the absence of TAC tie points due to the non-coincidence of TAC and ISI375 extrema (Fig. 3) while there is a good agreement between $\delta^{18}O_{atm}$ and $\delta^{18}O_{calcite}$ records. Therefore, we decide to increase up to 6 kyr the uncertainty attached to the four TAC age constraints between 600 and 550 ka BP (Fig. 2) and AICC2023 is rather following the $\delta^{18}O_{atm}$ based chronology, inducing older ages than AICC2012. At 765 ka BP, the discordance between $\delta O_2/N_2$ (and TAC) and $\delta^{18}O_{atm}$ based chronologies is likely due to the poor quality of the records from the lowermost part of the core. Over these oldest time periods, $\delta^{18}O_{atm}$, TAC and $\delta O_2/N_2$ were tied up respectively with precession, integrated insolation and insolation with a large uncertainty (6 to 10 kyr). This leads to a final chronology AICC2023 suggesting a larger chronological uncertainty than AICC2012 as well as younger ages (as per TAC and $\delta O_2/N_2$ chronologies) over MIS 18, and then older ages (as per $\delta^{18}O_{atm}$ chronology) over MIS 19.

Table 5. Description of the inconsistencies between $\delta O_2/N_2$, TAC and $\delta^{18}O_{atm}$ based chronologies. The age shift suggested by each dating tool with respect to AICC2012 age is detailed. The age position of the disagreement is given as per AICC2023. We did not highlight inconsistencies between $\delta O_2/N_2$ and TAC based chronologies as they remain within their respective orbital uncertainty.

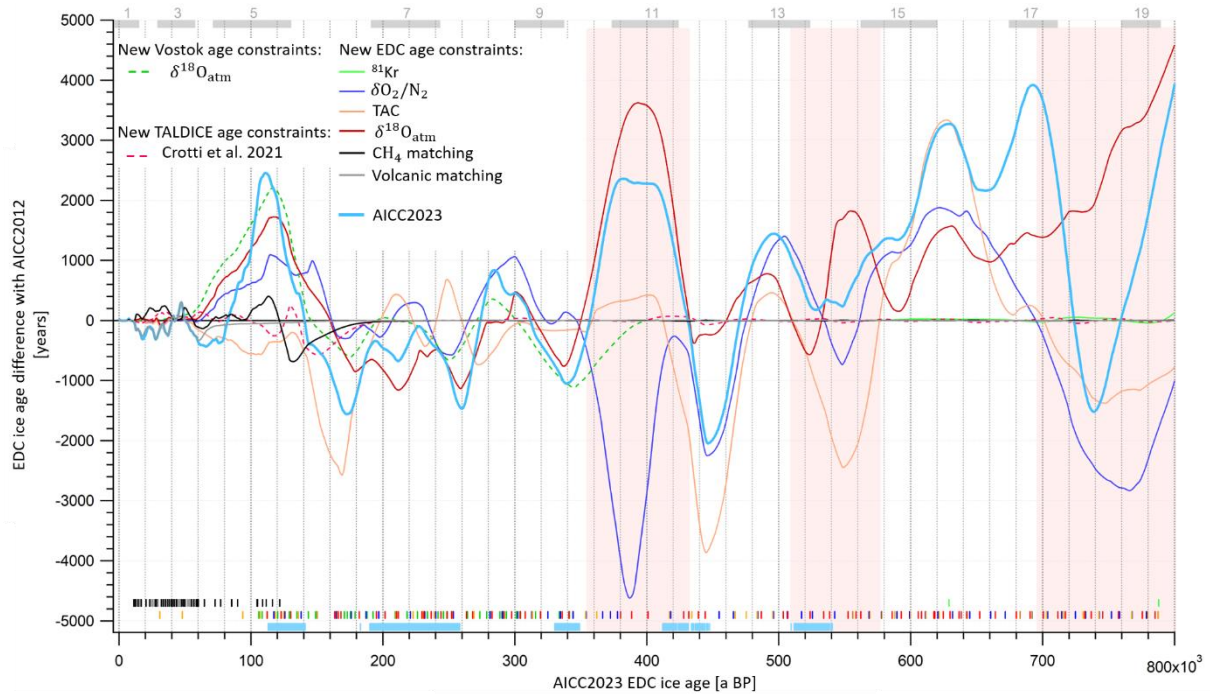|	$\delta^{18}O_{atm}$		
$\delta O_2/N_2$	Non-coherent	Non-coherent	Non-coherent
TAC	Coherent	Non-coherent	Non-coherent
Disagreement type	$\delta O_2/N_2$ chronology younger by 4,700 years than AICC2012	TAC (and $\delta O_2/N_2$) chronology younger by 2,400 (and 800) years than AICC2012	$\delta O_2/N_2$ (and TAC) chronology younger by 2,850 (and 1,300) years than AICC2012
	$\delta^{18}O_{atm}$ chronology older by 3,600 years than AICC2012	$\delta^{18}O_{atm}$ chronology older by 1,700 years than AICC2012	$\delta^{18}O_{atm}$ chronology older by 2,800 years than AICC2012
Interval of disagreement (ka BP)	430-350 (MIS 11)	580-510 (MIS 14)	800-700 (MIS 19-18)

Figure 7. EDC ice age difference between AICC2012 and different tests chronologies obtained with Paleochrono over the last 800 kyr. The ice age difference is calculated as per ("test chronology" – AICC2012). Two "test chronologies" are obtained either by addition of new Vostok $\delta^{18}O_{atm}$-$\delta^{18}O_{calcite}$ age constraints (green dotted line) or of stratigraphic and absolute TALDICE constraints between 470 and 129 ka BP from Crotti et al. (2021) (red dotted line). The other "test chronologies" are constructed by implementing either: (1) ^{81}Kr (green), (2) $\delta O_2/N_2$ (dark blue), (3) TAC (orange), (4) $\delta^{18}O_{atm}$ (red), (5) CH_4 tie points with NGRIP, EDML, TALDICE, Vostok (black) and (6) volcanic matching points with EDML and NGRIP (grey) to replace AICC2012 constraints. Vertical bars represent the corresponding age horizons. AICC2023 is obtained by implementing the new constraints all together (light blue line). Light blue vertical bars show new data collected by Grisart (2023) and presented in this work. The three largest inconsistencies between $\delta O_2/N_2$, TAC and $\delta^{18}O_{atm}$ chronologies are shown by red areas. Grey squares indicate interglacials from MIS 19 to MIS 1.

4.1.3 Final chronology and uncertainty

The new AICC2023 chronology suggests significant age shifts when compared to AICC2012 over old periods, including 3.8 and 5 kyr shifts towards older ages around 800 and 690 ka BP as well as a 2.1 kyr shift towards younger ages around 730 ka BP. The chronology is also modified over MIS 5 and MIS 11 where AICC2023 is about 2 kyr older than AICC2012. These 2 kyr shifts are induced by $\delta O_2/N_2$ and $\delta^{18}O_{atm}$ dating constraints and stratigraphic links over MIS 5 and by TAC and $\delta^{18}O_{atm}$ constraints over MIS 11. When averaged over the past 800 kyr, the chronological uncertainty is reduced from 1.7 kyr for AICC2012 to 900 years here. Still, it remains significant (above 2 kyr) over MIS 11 and in the lowermost part of the core, between 800 and 650 ka BP. Specifically, between 800 and 670 ka BP, the uncertainty associated with the new AICC2023 timescale sometimes is larger than the AICC2012 uncertainty (Fig. 8). This is caused by a larger relative error attached to $\delta O_2/N_2$ and TAC age constraints as well as by the eviction of the two redundant ^{10}Be age constraints at 780.3 and 798.3 ka BP associated with the Matuyama-Brunhes geomagnetic reversal event.
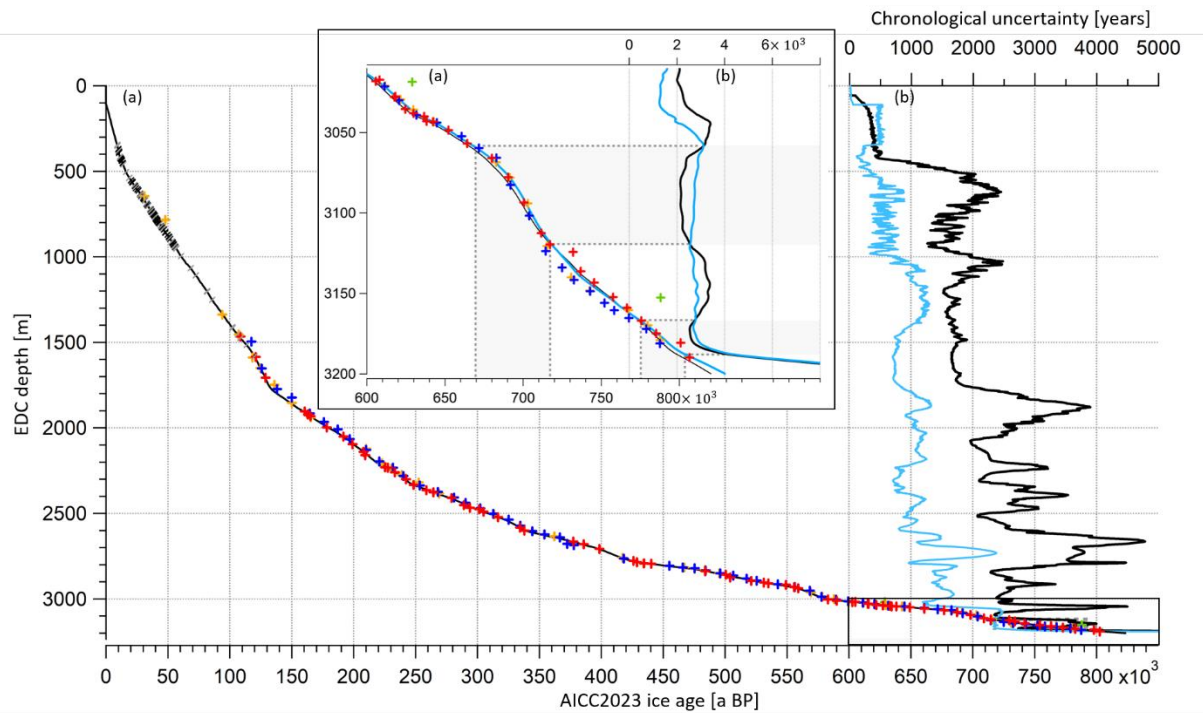
Figure 8. EDC ice age and uncertainty as a function of the depth. (a) EDC ice age (AICC2012 in black, AICC2023 in blue). (b) 1σ uncertainty (AICC2012 in black, AICC2023 in blue). Crosses and slashes represent new age constraints (ice stratigraphic links in black, gas stratigraphic links in grey, $\delta^{18}O_{atm}$ in red, $\delta O_2/N_2$ in blue, TAC in orange, ^{81}Kr in green). Inset is a zoom in between 800 and 600 ka BP. Grey rectangles frame periods where the new AICC2023 uncertainty is larger than AICC2012 uncertainty. See supplementary Fig. S13 for EDC gas age profile.

The age difference between ice and gas timescales (Δage) is of 3 kyr on average, reaching its largest values (~4 kyr) during the cold eras of MIS 12, 8, 6 and 4 (at 440, 260, 145 and 70 ka BP respectively, Fig. 9). A 4 kyr Δage is obtained at around 160 ka BP (Fig. 9), consistent with the use of new δ^{15}N data of Bréant et al. (2019) leading to a background scenario of LID that is 13 m smaller than the prior LID scenario used in AICC2012 between the depths of 1900 and 2000 m (Fig. 6). Using the definition of an interglacial period implying an EDC δD value surpassing the threshold of - 403 ‰ (EPICA Community members, 2004), we identify ten substages of interglacials (MIS 1, 5e, 7a, 7c, 7e, 9e, 11c, 15a, 15e and 19, Fig. 9). The average duration of these substages is reduced by 320 years with the new AICC2023 timescale in comparison with the AICC2012 chronology (Fig. 9). More specifically, MIS 5e to 15a are shorter while only MIS 15e and MIS 19 are longer. The largest decreases in duration affecting the Last Interglacial (MIS 5e) and MIS 11.c whose lengths are decreased from 16.3 to 15.1 kyr and from 31.1 to 30.1 kyr respectively, in agreement with the durations of 14.8 and 29.7 kyr proposed by Extier et al. (2018a).
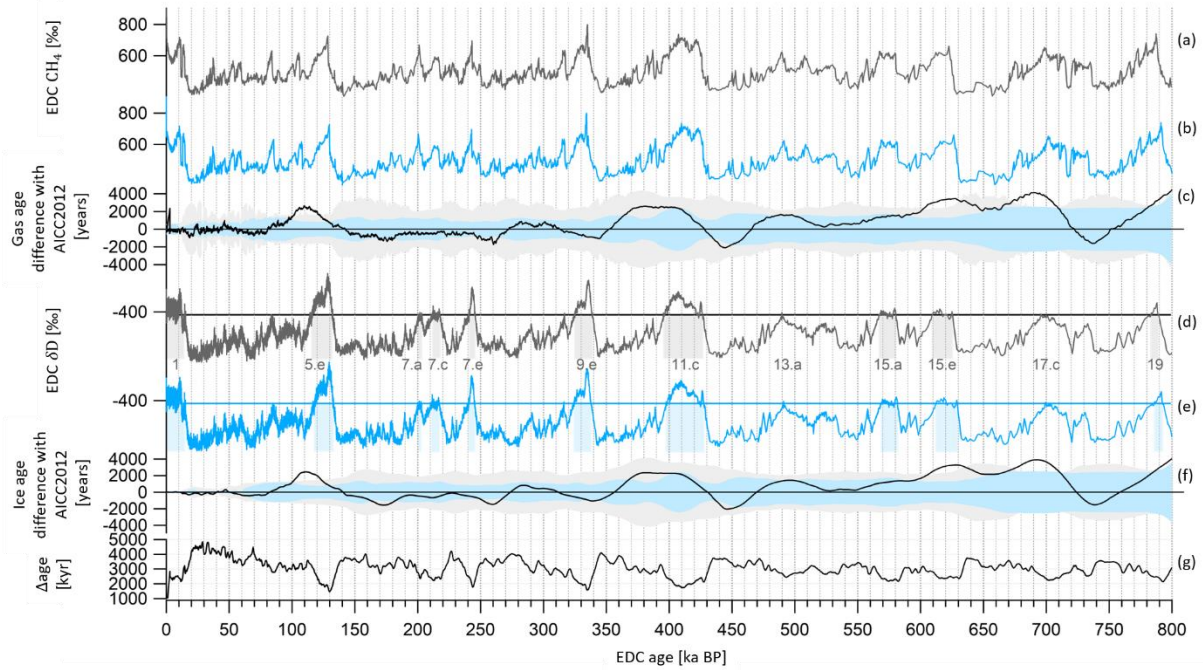
Figure 9. EDC gas and ice records on AICC2023 (blue) and AICC2012 (black) timescales over the last 800 kyr. (a) EDC CH_4 (Loulergue et al., 2008) on AICC2012 and (b) AICC2023 gas timescales. (c) Gas age difference AICC2023 – AICC2012. Grey and blue envelops are AICC2012 and AICC2023 chronological 1σ uncertainties respectively. (d) EDC δD (Jouzel et al., 2007) on AICC2012 and (e) AICC2023 ice timescales. Grey and blue rectangles indicate interglacial periods defined when δD is superior to the threshold of - 403 ‰ (horizontal lines) (EPICA members, 2004). Interglacials are numbered from MIS 1 to 19 (Berger et al., 2016). (f) Ice age difference AICC2023 – AICC2012. (g) Age difference between ice and gas AICC2023 timescales (Δage).

4.2 Comparison with other chronologies

4.2.1 MIS 5 (from 130 to 80 ka BP)

When Veres et al. (2013) presented the AICC2012 chronology over the last climatic cycle, they identified a disagreement with the Greenland timescale GICC05-modelext between 115 and 100 ka BP. The comparison between the Greenland $\delta^{18}O_{ice}$ record and the $\delta^{18}O_{calcite}$ from U-Th dated Alpine speleothems showed a delay up to 2.7 kyr during the Dansgaard Oeschger (D-O) events 23, 24 and 25. Later, this disagreement between abrupt changes in $\delta^{18}O_{ice}$ from NGRIP (Greenland surface temperature) and $\delta^{18}O_{calcite}$ from the Alps has been re-evaluated based on a different use of $\delta^{18}O_{atm}$ in ice core chronology and Extier et al. (2018a) presented a better agreement between the two records with an older NGRIP timescale than AICC2012 by ~2,200 years for D-O 23 to 25.

On Fig. 11, NGRIP $\delta^{18}O_{ice}$ record is represented on the AICC2023 timescale and is compared to ancient and novel records of $\delta^{18}O_{calcite}$ from Alpine speleothems (Boch et al., 2011; Moseley et al., 2020). Thanks to new $\delta O_2/N_2$ and $\delta^{18}O_{atm}$ age constraints, the new AICC2023 chronology is also older than AICC2012 between 115 and 100 ka BP and leads to an improved agreement between the records along with a reduction of the uncertainty. This amelioration is particularly visible over D-O warmings 23 and 24 where the difference between NALPS and NGRIP chronologies is reduced from ~2,000 years (AICC2012) to 430 and 325 years (AICC2023) respectively (Table 6).

26

The Greenland Interstadial (GI) 25 can be subdivided in three substages: GI-25a-b-c with GI-25a the earliest glacial so-called "rebound event" (Capron et al., 2010). This latter consists in a brief warm-wet excursion during the slow cooling trend of the longer GI-25 period, before jumping back to a cool-dry climate. The GI-25a warm-wet interval corresponds to a temperature increase in Greenland and continental Europe and hence identified by a positive excursion in NGRIP and NALPS δ^{18}O records (D-O 25 rebound) (Boch et al., 2011; Capron et al., 2012). At lower latitudes, this rebound likely affected the rainfall amount variations, as exhibited by the abrupt decrease in the δ^{18}O$_{calcite}$ from a U-Th dated Sardinian stalagmite from Bue Marino Cave (BMS1, Columbu et al., 2017). The 2 kyr shift of the new AICC2023 chronology towards older ages improves the coherency between NALPS, NGRIP and BMS1 timescales over the GI-25a onset (traceable in the δ^{18}O series, Fig. 10). The age discrepancy is reduced from ~3,600 years (between AICC2012 and BMS1 timescale) to 1,640 years (between AICC2023 and BMS1 timescale, Table 6).

Table 6. Timing of D-O warmings 23 and 24 and D-O 25 rebound event onset. The GICC05-modelext age uncertainty is undetermined.

Event	Timing (a BP) and error (years)					
	NGRIP ice core timescale				Speleothem timescale	
	GICC05-modelext (Wolff et al., 2010)	AICC2012 (Veres et al. 2013)	Extier et al. (2018a)	AICC2023 (This study)	BMS1 (Columbu et al. 2017)	NALPS (Boch et al. 2011)
D-O 23 warming	103 995	101 850 ± 1310	104 090 ± 1200	103 980 ± 930	Not recorded	103 550 ± 375
D-O 24 warming	108 250	105 850 ± 1330	108 010 ± 1200	107 975 ± 850	Not recorded	108 300 ± 450
D-O 25 rebound onset	110 960	108 100 ± 1410	110 280 ± 1200	110 120 ± 900	111 760 ± 450	111 780 ± 630
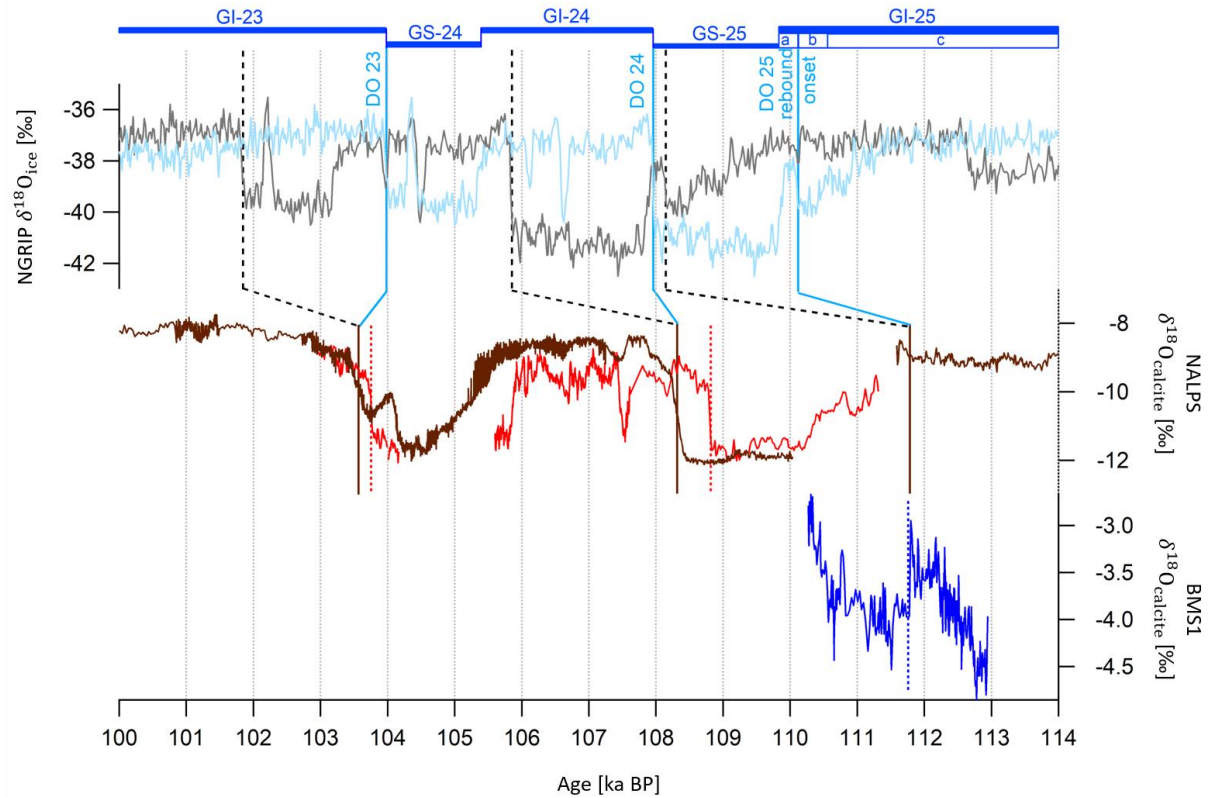
Figure 10. Northern Alpine speleothems (NALPS) and Bue Marino Stalagmite (BMS1) $\delta^{18}O_{calcite}$ records and NGRIP $\delta^{18}O_{ice}$ evolution between 114 and 100 ka BP. NGRIP $\delta^{18}O_{ice}$ data by Andersen et al. (2004) on AICC2012 (grey) and AICC2023 (blue) chronologies. NALPS $\delta^{18}O_{calcite}$ data by Moseley et al. (2020) (red) and Boch et al. (2011) (brown). BMS1 $\delta^{18}O_{calcite}$ data by Colombu et al. (2017) (dark blue). Vertical bars indicate D-O 25 rebound, D-O 24 and D-O 23 warmings at the onset of GI-25a warm-wet substage, GI-24 and GI-23. They correspond to abrupt increases in the NALPS $\delta^{18}O_{calcite}$ and NGRIP $\delta^{18}O_{ice}$ records and to a decrease in the BMS1 $\delta^{18}O_{calcite}$ series (for the GI-25a onset). Black dashed bars and blue bars show increases in $\delta^{18}O_{ice}$, respectively on AICC2012 and AICC2023 chronologies. Brown bars and red dotted bars show increases in NALPS $\delta^{18}O_{calcite}$ datasets. The blue dotted bar indicates the decrease in BMS1 $\delta^{18}O_{calcite}$. GI/GS (Greenland Stadials) boundaries and GI-25 subdivision are indicated on the new AICC2023 chronology by horizontal bars.

Between 128 and 103 ka BP, the comparison between the AICC2012 timescale and the novel Dome Fuji ice core DF2021 chronology indicates that AICC2012 is likely too young by up to 4 kyr. Here, thanks to new highly resolved $\delta O_2/N_2$ data and to the alignment of $\delta^{18}O_{atm}$ and $\delta^{18}O_{calcite}$ records, we improve the consistency between AICC2023 and DF2021, now agreeing within 1.7 kyr over MIS 5e (Fig. 11). With the new chronologies, the records of $\delta^{18}O_{atm}$ and $\delta O_2/N_2$ from Dome Fuji and EDC ice cores show synchronous variations between 140 and 115 ka BP although the $\delta O_2/N_2$ measurements from EDC are more scattered than DF data due to the use of smaller samples (see Sect. 1 in the Supplementary Material). However, δD records still are slightly discordant and EDC record lags DF by up to 1,700 years over MIS 5.e and at the onset of the Antarctic Isotope Maximum (AIM) 24 (Fig. 11), suggesting some remaining chronology problems (AIM 24 onset) or regional climatic differences (δD decrease over MIS 5.e). Between 180 and 150 ka BP, AICC2012 shows a better agreement with the DF2021 chronology than the new AICC2023 chronology which suggests younger ages as per TAC and $\delta^{18}O_{atm}$ dating constraints.

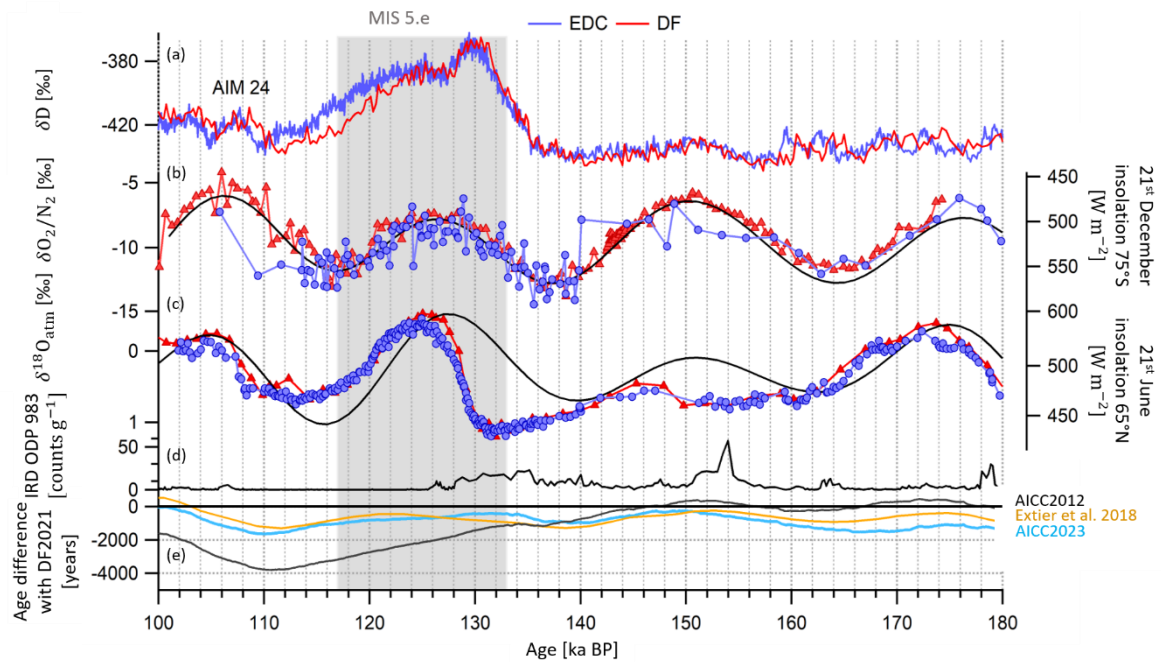**Figure 11. Evolution of EDC and DF records on AICC2023 and DF2021 chronologies between 180 and 100 ka BP.** (a) δD records from DF (red, Uemura et al., 2018) and EDC (blue, Jouzel et al., 2007). (b) $\delta O_2/N_2$ records from DF (red triangles, Oyabu et al., 2022) and EDC (blue circles, this work). (c) $\delta^{18}O_{atm}$ records from DF (red triangles, Kawamura et al., 2007) and EDC (blue circles, this work). DF and EDC records are represented on DF2021 and AICC2023 timescales. (d) IRD from ODP 983 (Barker et al., 2021). (e) Ice age difference between DF2021 and (i) AICC2023 (blue), (ii) Extier et al. (2018a) chronology (orange) and (iii) AICC2012 (black). The age difference is calculated as per EDC age – DF2021 age. DF2021 age is transferred onto EDC ice core via the volcanic synchronization of Fujita et al. (2015). Grey rectangle indicates MIS 5e.

4.2.2   MIS 11 (from 425 to 375 ka BP)

Over the time interval from 430 to 360 ka BP, encompassing MIS 11, the new AICC2023 chronology predicts older ages than AICC2012 (by up to 2 kyr) with a diminished uncertainty (from 3.9 to 1.7 kyr). This shift towards older ages is induced by $\delta^{18}O_{atm}$-$\delta^{18}O_{calcite}$ (Hulu, Sambao and Dongge caves) tie points at 377.3, 385.7 and 398.5 ka BP and by the TAC age constraint at 362.1 ka BP (Fig. 7, 12). As a result, two major rises in the EDC atmospheric CO_2 and CH_4 concentration records (corresponding to Carbon Dioxide Jumps, CDJ+ 11a.3 and 11a.4, labelled as per Nehrbass-Ahles et al., 2020) occur at 385.6 ± 1.4 and 389.8 ± 1.5 ka BP (Fig. 12). These two rapid jumps in CO_2 and CH_4 are better aligned with two abrupt decreases in the highly resolved $\delta^{18}O_{calcite}$ record of Zhao et al. (2019) from Yongxing cave (independently dated with ^{230}Th at 386.4 ± 3.1 and 390.0 ± 3.0 ka BP) than when using the AICC2012 chronology (improvement by ~800 years). Such millennial-scale synchronicity is expected between CH_4 and $\delta^{18}O_{calcite}$ series from Chinese speleothems as they both are influenced by Asian monsoon area displacements (and associated methane emissions from wetlands) (Sánchez Goñi et al., 2008).
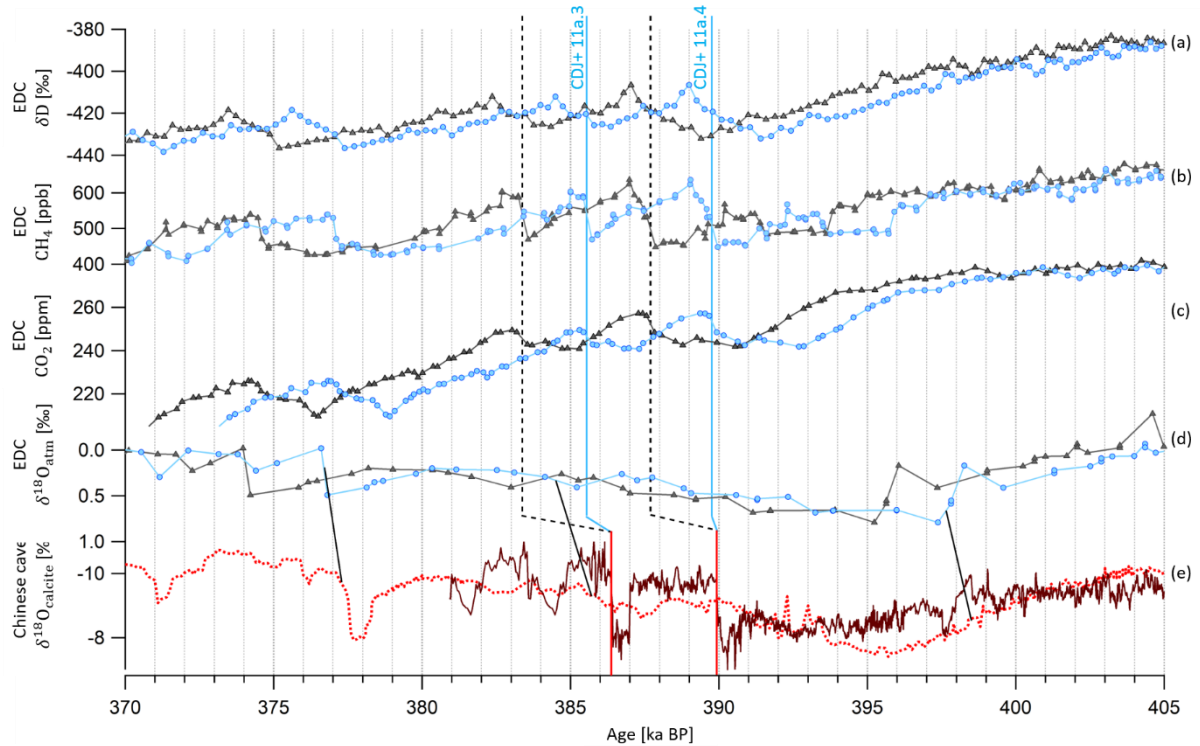
29

Figure 12. Evolution of climate tracers from EDC ice core and Yongxing cave stalagmites between 405 and 370 ka BP. EDC records of (a) δD, (b) CH_4 (Nehrbass-Ahles et al., 2020), (c) CO_2 (Nehrbass-Ahles et al., 2020) and (d) $\delta^{18}O_{atm}$ on AICC2012 (grey triangles) and AICC2023 (blue circles) chronologies. (e) Speleothems $\delta^{18}O_{calcite}$ from Hulu, Dongge and Sambao cave, used to constrain AICC2023 (dashed red curve, Cheng et al. 2016) and from Yongxing cave, independently dated with ^{230}Th dating and annual band counting (brown plain curve, Zhao et al. 2019). CDJ+ are labelled as per Nehrbass-Ahles et al. (2020). Dashed black and blue vertical bars show jumps in CO_2 respectively on AICC2012 and AICC2023 chronologies, red vertical bars show corresponding decreases in $\delta^{18}O_{calcite}$. Black lines show the three tie points between $\delta^{18}O_{atm}$ and $\delta^{18}O_{calcite}$ (Cheng et al., 2016) used to constrain AICC2023.

4.2.3 MIS 19 (from 780 to 760 ka BP)

The Matuyama-Brunhes event (geomagnetic field reversal) is reflected by a globally synchronous event in the ^{10}Be signal: an abrupt termination of the large ^{10}Be peak following a long-term increasing trend recorded in both ice and sedimentary cores (Giaccio et al., 2023). The ^{40}Ar/^{39}Ar age constrained chronology of a lacustrine succession from Sulmona basin (Giaccio et al., 2023) gives an age of 770.9 $\pm$ 1.6 ka BP for the ^{10}Be peak termination. The new AICC2023 chronology provides an estimate of 767.3 $\pm$ 3 ka BP for the same ^{10}Be peak termination, an age which is closer to the ^{40}Ar/^{39}Ar age evaluation than the AICCC2012 chronology estimate (766.2 $\pm$ 3 ka BP, Fig. 13). The new AICC2023 chronology indeed indicates an increasing older age than AICC2012 over MIS 19 (from 790 to 761 ka BP) due to the new $\delta^{18}O_{atm}$ based timescale (Fig. 7).

We acknowledge that the Chiba composite section also provides high-resolution ^{10}Be record, as the Montalbano Jonico marine section (Simon et al. 2017), the Sulmona basin succession and the EDC ice core do. Although, the ^{10}Be flux records of Sulmona and EDC show a similar pattern and the same asymmetrical shape (i.e., slow increase followed by an abrupt ^{10}Be peak termination), the sharp termination is less obvious in the Montalbano Jonico and Chiba records. In addition, Chiba and Montalbano Jonico records are shallow marine deposits, hence expression of paleoclimatic proxies can be amplified and/or hampered by fluvial input (Nomade
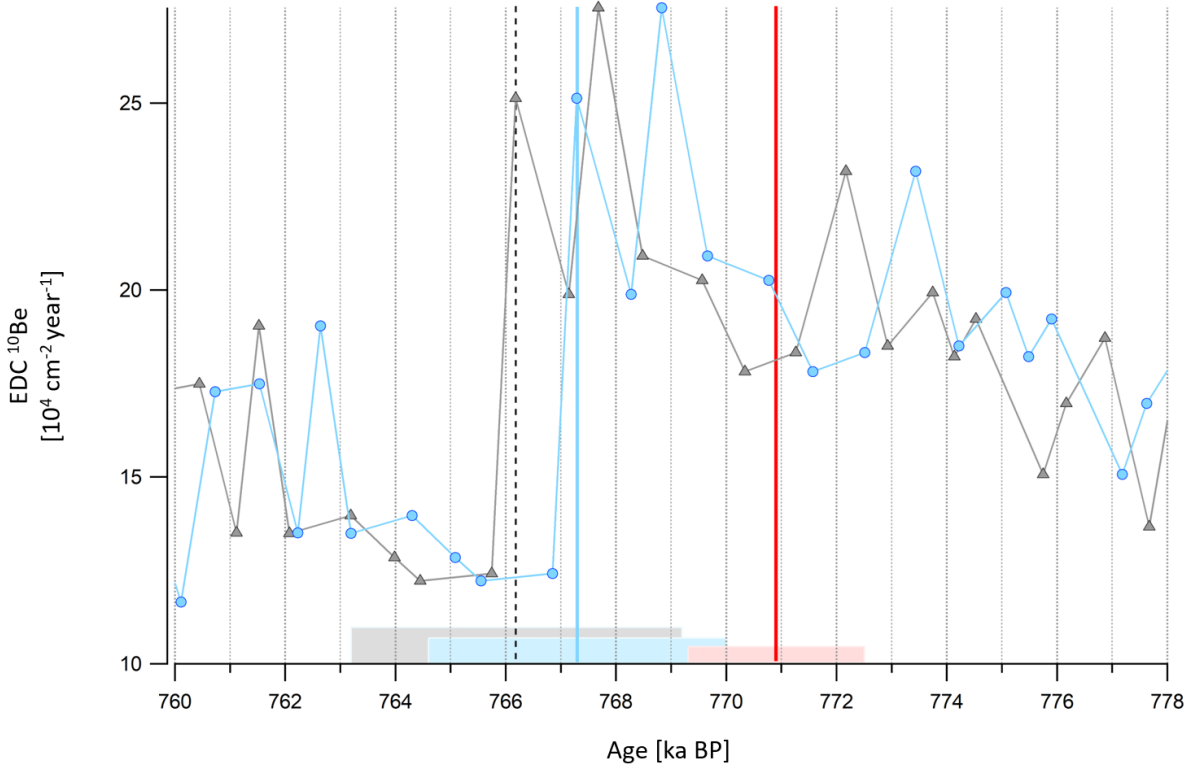
Figure 13. EDC ^{10}Be record on AICC2012 and AICC2023 chronologies between 778 and 760 ka BP. Grey and blue vertical bars indicate the age of the abrupt EDC ^{10}Be peak termination respectively on AICC2012 (grey triangles) and AICC2023 (blue circles) chronologies. The grey and blue horizontal squares correspond to AICC2012 and AICC2023 2σ confidence intervals (±3 and ±2.7 ka respectively). The red vertical bar and horizontal square show the ^{10}Be peak termination age and its 2σ confidence interval (770.9 ± 1.6 ka BP, Giaccio et al. 2023).

Conclusions

In this study, we have established a new reference chronology for EDC ice core, AICC2023 covering the last 800 kyr, that is consistent with the official GICC05 timescale over the last 60 kyr. A valuable update of the chronology construction has been the compilation of chronological and glaciological information including new age markers from recent high resolution measurements on the EDC ice core. As a result, the chronological uncertainty is reduced from 1.7 kyr in AICC2012 (standard deviation of 995 years) to 900 years on average in AICC2023 (standard deviation of 720 years). 90 % of the new AICC2023 timescale is associated with an uncertainty lower than 2 kyr, against only 60 % in the AICC2012 chronology. First, the distinct orbital chronologies derived from $\delta O_2/N_2$, TAC and $\delta^{18}O_{atm}$ are coherent within their respective uncertainties except over three periods including MIS 11 and MIS 19. Second, new $\delta^{15}N$ measurements along with new sensitivity tests with the firn densification model described by Bréant et al. (2017) and adapted for the EDC ice core provide the most plausible evolution of LID at EDC over the last 800 kyr.

The majorities of the age disparities observed between AICC2023 and AICC2012 chronologies are smaller than 500 years (median), hence minor considering the average uncertainty of AICC2012 (1.7 kyr). Exceptions are significant age shifts reaching 3.4, 3.8 and 5 kyr towards older ages respectively suggested over MIS 15, MIS 17 and MIS 19. However, most of these age discrepancies lead to an improved coherency between the new EDC timescale and independent absolute chronologies derived for other climate archives especially over the following periods: MIS 5, MIS 11 and MIS 19.

We have identified time intervals where building the chronology is more complicated such as TVI (from 540 to 456 ka BP) and from 800 to 600 ka BP, corresponding to the lowermost section of the core and we would like to draw attention to the requirement for new measurements over these periods. In particular, the links between the variability of $\delta O_2/N_2$ and TAC records and their orbital targets are not obvious over the 800 – 600 ka BP period (Fig. 1). This may be due to bad quality of the ice and/or diffusion of gases through the ice matrix (Bereiter et al., 2009). The imprecision of the signal may also be partially explained by the limited temporal resolution of the existing dataset in this deep section. To address these issues, highly resolved $\delta O_2/N_2$ and TAC measurements are needed in the lowermost section of EDC ice core. In addition, $\delta O_2/N_2$ from ice samples over the period covering TVI should also be analyzed to investigate the mismatch between old and new datasets (Fig. 1).

A final important aspect would be to further extend the Paleochrono dating experiment by implementing other ice cores such as Dome Fuji, WAIS Divide and NEEM (North Greenland Eemian), for which a large amount of chronological and glaciological information is now available.

Code availability

The input and output files of the AICC2023 Paleochrono run are available on GitHub. They contain age markers used to construct AICC2023 (including both updated and old ones).
https://github.com/parrenin/paleochrono/tree/master/AICC2023.

Data availability

A folder is available for each site in the PANGAEA data repository. It includes new gas and ice age scales and their uncertainties, new gas data along with background and analyzed scenarios for accumulation rate, thinning function and LID. A correspondence between AICC2023 and WD2014 age models is also given.
https://doi.pangaea.de/10.1594/PANGAEA.961017
The new $\delta^{18}O_{atm}$ and $\delta O_2/N_2$ datasets for EDC are also available in the PANGAEA data repository:
https://doi.pangaea.de/10.1594/PANGAEA.961023

885 **References**

886 Alley, R. B.: Firn densification by grain-boundary sliding: a first model, Le Journal de Physique Colloque, 48, 1-
887 249, DOI:10.1051/JPHYSCOL:1987135, 1987.

888 Andersen, K. K., Azuma, N., Barnola, J.-M., Bigler, M., Biscaye, P., Caillon, N., Chappellaz, J., Clausen, H. B.,
889 Dahl-Jensen, D., Fischer, H., Flückiger, J., Fritzsche, D., Fujii, Y., Goto-Azuma, K., Grønvold, K., Gundestrup,
890 N. S., Hansson, M., Huber, C., Hvidberg, C. S., Johnsen, S. J., Jonsell, U., Jouzel, J., Kipfstuhl, S., Landais, A.,
891 Leuenberger, M., Lorrain, R., Masson-Delmotte, V., Miller, H., Motoyama, H., Narita, H., Popp, T., Rasmussen,
892 S. O., Raynaud, D., Rothlisberger, R., Ruth, U., Samyn, D., Schwander, J., Shoji, H., Siggard-Andersen, M.-L.,
893 Steffensen, J. P., Stocker, T., Sveinbjörnsdóttir, A. E., Svensson, A., Takata, M., Tison, J.-L., Thorsteinsson, Th.,
894 Watanabe, O., Wilhelms, F., White, J. W. C., and members, N. G. I. C. P.: High-resolution record of Northern
895 Hemisphere climate extending into the last interglacial period, Nature, 431, 147–151, DOI:10.1038/nature02805,
896 2004.

897 Andersen, K. K., Svensson, A., Johnsen, S. J., Rasmussen, S. O., Bigler, M., Röthlisberger, R., Ruth, U., Siggaard-
898 Andersen, M.-L., Peder Steffensen, J., Dahl-Jensen, D., Vinther, B. M., and Clausen, H. B.: The Greenland Ice
899 Core Chronology 2005, 15–42ka. Part 1: constructing the time scale, Quat. Sci. Rev., 25, 3246–3257,
900 DOI:10.1016/j.quascirev.2006.08.002, 2006.

901 Barker, S (2021): Planktic foraminiferal and Ice Rafted Debris (IRD) counts from ODP Site 983:
902 DOI:10.1594/PANGAEA.929721, last access: 8 January 2023.

903 Arnaud, L., Barnola, J. M., and Duval, P.: Physical modeling of the densification of snow/firn and ice in the upper
904 part of polar ice sheets, Physics of Ice Core Records, 285-305, http://hdl.handle.net/2115/32472, 2000.

905 Arthern, R. J., Vaughan, D. G., Rankin, A. M., Mulvaney, R., and Thomas, E. R.: In situ measurements of Antarctic
906 snow compaction compared with predictions of models, J. Geophys. Res. Earth Surf., 115, 3011,
907 DOI:10.1029/2009JF001306, 2010.

908 Augustin, L., Barbante, C., Barnes, P. R. F., Barnola, J. M., Bigler, M., Castellano, E., Cattani, O., Chappellaz, J.,
909 Dahl-Jensen, D., Delmonte, B., Dreyfus, G., Durand, G., Falourd, S., Fischer, H., Flückiger, J., Hansson, M. E.,
910 Huybrechts, P., Jugie, G., Johnsen, S. J., Jouzel, J., Kaufmann, P., Kipfstuhl, J., Lambert, F., Lipenkov, V. Y.,
911 Littot, G. C., Longinelli, A., Lorrain, R., Maggi, V., Masson-Delmotte, V., Miller, H., Mulvaney, R., Oerlemans,
912 J., Oerter, H., Orombelli, G., Parrenin, F., Peel, D. A., Petit, J. R., Raynaud, D., Ritz, C., Ruth, U., Schwander, J.,
913 Siegenthaler, U., Souchez, R., Stauffer, B., Steffensen, J. P., Stenni, B., Stocker, T. F., Tabacco, I. E., Udisti, R.,
914 van de Wal, R. S. W., van den Broeke, M., Weiss, J., Wilhelms, F., Winther, J. G., Wolff, E. W., and Zucchelli,
915 M.: Eight glacial cycles from an Antarctic ice core, Nature, 429, 623–628, DOI:10.1038/nature02599, 2004.

916 Baglin, C. M.: Nuclear Data Sheets for A = 81, Nucl. Data Sheets, 109, 2257–2437,
917 DOI:10.1016/J.NDS.2008.09.001, 2008.

918 Barnola, J. -M, Pimienta, P., Raynaud, D., and Korotkevich, Y. S.: CO_2-climate relationship as deduced from the
919 Vostok ice core: a re-examination based on new measurements and on a re-evaluation of the air dating, Tellus B:
920 Chem. Phys. Meteorol., 43, 83–90, DOI:10.1034/J.1600-0889.1991.T01-1-00002.X, 1991.

921 Baumgartner, M., Kindler, P., Eicher, O., Floch, G., Schilt, A., Schwander, J., Spahni, R., Capron, E., Chappellaz,
922 J., Leuenberger, M., Fischer, H., and Stocker, T. F.: NGRIP CH_4 concentration from 120 to 10 kyr before present
923 and its relation to a $\delta 15N$ temperature reconstruction from the same ice core, Clim. Past, 10, 903–920,
924 DOI:10.5194/CP-10-903-2014, 2014.

925 Bazin, L., Landais, A., Lemieux-Dudon, B., Toyé Mahamadou Kele, H., Veres, D., Parrenin, F., Martinerie, P.,
926 Ritz, C., Capron, E., Lipenkov, V., Loutre, M.-F., Raynaud, D., Vinther, B., Svensson, A., Rasmussen, S. O.,
927 Severi, M., Blunier, T., Leuenberger, M., Fischer, H., Masson-Delmotte, V., Chappellaz, J., and Wolff, E.: An
928 optimized multi-proxy, multi-site Antarctic ice and gas orbital chronology (AICC2012): 120–800 ka, Clim. Past,
929 9, 1715–1731, DOI:10.5194/cp-9-1715-2013, 2013.

930 Bazin, L., Landais, A., Capron, E., Masson-Delmotte, V., Ritz, C., Picard, G., Jouzel, J., Dumont, M., Leuenberger,
931 M., and Prié, F.: Phase relationships between orbital forcing and the composition of air trapped in Antarctic ice
932 cores, Clim. Past, 12, 729–748, DOI:10.5194/cp-12-729-2016, 2016.

933 Bender, M. L.: Orbital tuning chronology for the Vostok climate record supported by trapped gas composition,
934 Earth Planet. Sci. Lett., 204, 275–289, DOI:10.1016/S0012-821X(02)00980-9, 2002.

935 Bender, M. L., Barnett, B., Dreyfus, G., Jouzel, J., and Porcelli, D.: The contemporary degassing rate of $40Ar$ from
936 the solid Earth, Proc. Natl. Acad. Sci. U.S.A., 105, 8232–8237, DOI:10.1073/PNAS.0711679105, 2008.

937 Bereiter, B., Schwander, J., Lüthi, D., and Stocker, T. F.: Change in CO_2 concentration and O_2/N_2 ratio in ice
938 cores due to molecular diffusion, Geophys. Res. Lett., 36, DOI:10.1029/2008GL036737, 2009.

939 Berger, A.: Long-Term Variations of Daily Insolation and Quaternary Climatic Changes, J. Atmos. Sci., 35, 2362–
940 2367, DOI:10.1175/1520-0469(1978)035<2362:LTVODI>2.0.CO;2, 1978.

941 Berger, B., Crucifix, M., Hodell, D. A., Mangili, C., McManus, J. F., Otto-Bliesner, B., Pol, K., Raynaud, D.,
942 Skinner, L. C., Tzedakis, P. C., Wolff, E. W., Yin, Q. Z., Abe-Ouchi, A., Barbante, C., Brovkin, V., Cacho, I.,
943 Capron, E., Ferretti, P., Ganopolski, A., Grimalt, J. O., Hönisch, B., Kawamura, K. A., Landais, A., Margari, V.,
944 Martrat, B., Masson-Delmotte, V., Mokeddem, Z., Parrenin, F., Prokopenko, A. A., Rashid, H., Schulz, M., and
945 Vazquez Riveiros, N.: Interglacials of the last 800,000 years, Rev. Geophys., 54, 162–219,
946 DOI:10.1002/2015RG000482, 2016.

947 Boch, R., Cheng, H., Spötl, C., Edwards, R. L., Wang, X., and Häuselmann, Ph.: NALPS: a precisely dated
948 European climate record 120–60 ka, Clim. Past, 7, 1247–1259, DOI:10.5194/cp-7-1247-2011, 2011.

949 Bréant, C., Martinerie, P., Orsi, A., Arnaud, L., and Landais, A.: Modelling firn thickness evolution during the last
950 deglaciation: constraints on sensitivity to temperature and impurities, Clim. Past, 13, 833–853, DOI:10.5194/cp-
951 13-833-2017, 2017.

952 Bréant, C., Landais, A., Orsi, A., Martinerie, P., Extier, T., Prié, F., Stenni, B., Jouzel, J., Masson-Delmotte, V.,
953 and Leuenberger, M.: Unveiling the anatomy of Termination 3 using water and air isotopes in the Dome C ice
954 core, East Antarctica, Quat. Sci. Rev., 211, 156–165, DOI:10.1016/J.QUASCIREV.2019.03.025, 2019.

955 Buizert, C.: The Ice Core Gas Age-Ice Age Difference as a Proxy for Surface Temperature, Geophys. Res. Lett.,
956 48, e2021GL094241, DOI:10.1029/2021GL094241, 2021.

957 Buizert, C., Sowers, T., and Blunier, T.: Assessment of diffusive isotopic fractionation in polar firn, and application
958 to ice core trace gas records, Earth Planet. Sci. Lett., 361, 110–119, DOI:10.1016/J.EPSL.2012.11.039, 2013.

959 Buizert, C., Baggenstos, D., Jiang, W., Purtschert, R., Petrenko, V. V., Lu, Z. T., Müller, P., Kuhl, T., Lee, J.,
960 Severinghaus, J. P., and Brook, E. J.: Radiometric 81Kr dating identifies 120,000-year-old ice at Taylor Glacier,
961 Antarctica, Proc. Natl. Acad. Sci. U.S.A., 111, 6876–6881, DOI:10.1073/pnas.1320329111, 2014.

962 Caillon, N., Jouzel, J., Severinghaus, J. P., Chappellaz, J., and Blunier, T.: A novel method to study the phase
963 relationship between Antarctic and Greenland climate, Geophys. Res. Lett., 30, DOI:10.1029/2003GL017838,
964 2003.

965 Capron, E., Landais, A., Chappellaz, J., Schilt, A., Buiron, D., Dahl-Jensen, D., Johnsen, S. J., Jouzel, J., Lemieux-
966 Dudon, B., Loulergue, L., Leuenberger, M., Masson-Delmotte, V., Meyer, H., Oerter, H., and Stenni, B.:
967 Millennial and sub-millennial scale climatic variations recorded in polar ice cores over the last glacial period,
968 Clim. Past, 6, 345–365, DOI:10.5194/CP-6-345-2010, 2010.

969 Capron, E., Landais, A., Chappellaz, J., Buiron, D., Fischer, H., Johnsen, S. J., Jouzel, J., Leuenberger, M.,
970 Masson-Delmotte, V., and Stocker, T. F.: A global picture of the first abrupt climatic event occurring during the
971 last glacial inception, Geophys. Res. Lett., 39, DOI:10.1029/2012GL052656, 2012.

972 Capron, E., Landais, A., Buiron, D., Cauquoin, A., Chappellaz, J., Debret, M., Jouzel, J., Leuenberger, M.,
973 Martinerie, P., Masson-Delmotte, V., Mulvaney, R., Parrenin, F., and Prié, F.: Glacial-interglacial dynamics of
974 Antarctic firn columns: Comparison between simulations and ice core air-$\delta15N$ measurements, Clim. Past, 9, 983–
975 999, DOI:10.5194/CP-9-983-2013, 2013.

976 Cheng, H., Edwards, R. L., Sinha, A., Spötl, C., Yi, L., Chen, S., Kelly, M., Kathayat, G., Wang, X., Li, X., Kong,
977 X., Wang, Y., Ning, Y., and Zhang, H.: The Asian monsoon over the past 640,000 years and ice age terminations,
978 Nature, 534, 640–646, DOI:10.1038/nature18591, 2016.

979 Columbu, A., Drysdale, R., Capron, E., Woodhead, J., De Waele, J., Sanna, L., Hellstrom, J., and Bajo, P.: Early
980 last glacial intra-interstadial climate variability recorded in a Sardinian speleothem, Quat. Sci. Rev., 169, 391–397,
981 DOI:10.1016/J.QUASCIREV.2017.05.007, 2017.

982 Crotti, I., Landais, A., Stenni, B., Bazin, L., Parrenin, F., Frezzotti, M., Ritterbusch, F., Lu, Z. T., Jiang, W., Yang,
983 G. M., Fourré, E., Orsi, A., Jacob, R., Minster, B., Prié, F., Dreossi, G., and Barbante, C.: An extension of the
984 TALDICE ice core age scale reaching back to MIS 10.1, Quat. Sci. Rev., 266, 107078,
985 DOI:10.1016/J.QUASCIREV.2021.107078, 2021.

986 Dansgaard, W. and Johnsen, S. J.: A Flow Model and a Time Scale for the Ice Core from Camp Century,
987 Greenland, J. Glaciol., 8, 215–223, DOI:10.3189/S0022143000031208, 1969.

988 Dong, X. Z., Ritterbusch, F., Chu, Y. Q., Gu, J. Q., Hu, S. M., Jiang, W., Lu, Z. T., Yang, G. M., and Zhao, L.:
989 Dual Separation of Krypton and Argon from Environmental Samples for Radioisotope Dating, Anal. Chem., 91,
990 13576–13581, DOI:10.1021/ACS.ANALCHEM.9B02716, 2019.

991 Dreyfus, G. B., Parrenin, F., Lemieux-Dudon, B., Durand, G., Masson-Delmotte, V., Jouzel, J., Barnola, J. M.,
992 Panno, L., Spahni, R., Tisserand, A., Siegenthaler, U., and Leuenberger, M.: Anomalous flow below 2700 m in
993 the EPICA Dome C ice core detected using $\delta18O$ of atmospheric oxygen measurements, Clim. Past, 3, 341–353,
994 DOI:10.5194/CP-3-341-2007, 2007.

995 Dreyfus, G. B., Raisbeck, G. M., Parrenin, F., Jouzel, J., Guyodo, Y., Nomade, S., and Mazaud, A.: An ice core
996 perspective on the age of the Matuyama–Brunhes boundary, Earth Planet. Sci. Lett., 274, 151–156,
997 DOI:10.1016/J.EPSL.2008.07.008, 2008.

998 Dreyfus, G. B., Jouzel, J., Bender, M. L., Landais, A., Masson-Delmotte, V., and Leuenberger, M.: Firn processes
999 and δ15N: potential for a gas-phase climate proxy, Quat. Sci. Rev., 29, 28–42,
1000 DOI:10.1016/j.quascirev.2009.10.012, 2010.

1001 Epifanio, J. A., Brook, E. J., Buizert, C., Edwards, J. S., Sowers, T. A., Kahle, E. C., Severinghaus, J. P., Steig, E.
1002 J., Winski, D. A., Osterberg, E. C., Fudge, T. J., Aydin, M., Hood, E., Kalk, M., Kreutz, K. J., Ferris, D. G., and
1003 Kennedy, J. A.: The SP19 chronology for the South Pole Ice Core - Part 2: Gas chronology, Δage, and smoothing
1004 of atmospheric records, Clim. Past, 16, 2431–2444, DOI:10.5194/CP-16-2431-2020, 2020.

1005 Extier, T., Landais, A., Bréant, C., Prié, F., Bazin, L., Dreyfus, G., Roche, D. M., and Leuenberger, M.: On the
1006 use of δ18Oatm for ice core dating, Quat. Sci. Rev., 185, 244–257, DOI:10.1016/J.QUASCIREV.2018.02.008,
1007 2018a.

1008 Extier, T., Landais, A., Bréant, C., Prié, F., Bazin, L., Dreyfus, G., Roche, D. M., and Leuenberger, M. C.: δ18Oatm
1009 records between 100-800 ka from EPICA Dome C ice core, PANGAEA, DOI:10.1594/PANGAEA.887323,
1010 2018b.

1011 Extier, T., Landais, A., Bréant, C., Prié, F., Bazin, L., Dreyfus, G., Roche, D. M., and Leuenberger, M. C.: δO2/N2
1012 records between 100-800 ka from EPICA Dome C ice core, PANGAEA, DOI:10.1594/PANGAEA.887326,
1013 2018c.

1014 Freitag, J., Kipfstuhl, S., Laepple, T., and Wilhelms, F.: Impurity-controlled densification: a new model for
1015 stratified polar firn, J. Glaciol., 59, 1163–1169, DOI:10.3189/2013JOG13J042, 2013.

1016 Fujita, S., Parrenin, F., Severi, M., Motoyama, H., and Wolff, E. W.: Volcanic synchronization of Dome Fuji and
1017 Dome C Antarctic deep ice cores over the past 216 kyr, Clim. Past, 11, 1395–1416, DOI:10.5194/CP-11-1395-
1018 2015, 2015.

1019 Giaccio, B., Zanchetta, G., Galli, P., Nomade, S., Regattieri, E., and Sagnotti, L.: The Quaternary evolution of
1020 Sulmona basin, central Italy, https://inquaroma2023.org/wp-content/uploads/2022/01/5-Post.pdf, last access: 10
1021 September 2023.

1022 Goujon, C., Barnola, J. M., and Ritz, C.: Modeling the densification of polar firn including heat diffusion:
1023 Application to close-off characteristics and gas isotopic fractionation for Antarctica and Greenland sites, J.
1024 Geophys. Res. Atmos., 108, 4792, DOI:10.1029/2002JD003319, 2003.

1025 Grachev, A. M. and Severinghaus, J. P.: Determining the thermal diffusion factor for 40Ar/36Ar in air to aid
1026 paleoreconstruction of abrupt climate change, J. Phys. Chem. A., 107, 4636–4642, DOI:10.1021/JP027817U,
1027 2003.

1028 Grisart, A.: Étude à haute résolution des cycles hydrologiques et climatiques à partir d'une carotte de glace
1029 d'Antarctique avec un focus sur les déglaciations, Université Paris-Saclay, https://theses.hal.science/tel-04042459,
1030 2023.

1031 Heaton, T. J., Bard, E., Ramsey, C. B., Butzin, M., Köhler, P., Muscheler, R., Reimer, P. J., and Wacker, L.:
1032 Radiocarbon: A key tracer for studying Earth's dynamo, climate system, carbon cycle, and Sun, Science, 374,
1033 6568, DOI:10.1126/SCIENCE.ABD7096, 2021.

1034 Herron, M. M. and Langway, C. C.: Firn densification: an empirical model, J. Glaciol., 25,
1035 DOI:10.3189/S0022143000015239, 1980.

1036 Hörhold, M. W., Laepple, T., Freitag, J., Bigler, M., Fischer, H., and Kipfstuhl, S.: On the impact of impurities on
1037 the densification of polar firn, Earth Planet. Sci. Lett., 325–326, 93–99, DOI:10.1016/J.EPSL.2011.12.022, 2012.

Jiang, W., Hu, S. M., Lu, Z. T., Ritterbusch, F., and Yang, G. min: Latest development of radiokrypton dating – A tool to find and study paleogroundwater, Quat. Int., 547, 166–171, DOI:10.1016/J.QUAINT.2019.04.025, 2020.

Jouzel, J., Hoffmann, G., Parrenin, F., and Waelbroeck, C.: Atmospheric oxygen 18 and sea-level changes, Quat. Sci. Rev., 21, 307–314, DOI:10.1016/S0277-3791(01)00106-8, 2002.

Jouzel, J., Masson-Delmotte, V., Cattani, O., Dreyfus, G., Falourd, S., Hoffmann, G., Minster, B., Nouet, J., Barnola, J. M., Chappellaz, J., Fischer, H., Gallet, J. C., Johnsen, S., Leuenberger, M., Loulergue, L., Luethi, D., Oerter, H., Parrenin, F., Raisbeck, G., Raynaud, D., Schilt, A., Schwander, J., Selmo, E., Souchez, R., Spahni, R., Stauffer, B., Steffensen, J. P., Stenni, B., Stocker, T. F., Tison, J. L., Werner, M., and Wolff, E. W.: Orbital and millennial antarctic climate variability over the past 800,000 years, Science, 317, 793–796, DOI:10.1126/SCIENCE.1141038, 2007.

Kawamura, K., Parrenin, F., Lisiecki, L., Uemura, R., Vimeux, F., Severinghaus, J. P., Hutterli, M. A., Nakazawa, T., Aoki, S., Jouzel, J., Raymo, M. E., Matsumoto, K., Nakata, H., Motoyama, H., Fujita, S., Goto-Azuma, K., Fujii, Y., and Watanabe, O.: Northern Hemisphere forcing of climatic cycles in Antarctica over the past 360,000 years, Nature, 448, 912–916, DOI:10.1038/nature06015, 2007.

Kuipers Munneke, P., Ligtenberg, S. R. M., Noël, B. P. Y., Howat, I. M., Box, J. E., Mosley-Thompson, E., McConnell, J. R., Steffen, K., Harper, J. T., Das, S. B., and Van Den Broeke, M. R.: Elevation change of the Greenland Ice Sheet due to surface mass balance and firn processes, 1960-2014, Cryosphere, 9, 2009–2025, DOI:10.5194/TC-9-2009-2015, 2015.

Landais, A., Chappellaz, J., Delmotte, M., Jouzel, J., Blunier, T., Bourg, C., Caillon, N., Cherrier, S., Malaizé, B., Masson-Delmotte, V., Raynaud, D., Schwander, J., and Steffensen, J. P.: A tentative reconstruction of the last interglacial and glacial inception in Greenland based on new gas measurements in the Greenland Ice Core Project (GRIP) ice core, J. Geophys. Res. Atmos., 108, DOI:10.1029/2002JD003147, 2003.

Landais, A., Barnola, J. M., Kawamura, K., Caillon, N., Delmotte, M., Van Ommen, T., Dreyfus, G., Jouzel, J., Masson-Delmotte, V., Minster, B., Freitag, J., Leuenberger, M., Schwander, J., Huber, C., Etheridge, D., and Morgan, V.: Firn-air $\delta 15N$ in modern polar sites and glacial–interglacial ice: a model-data mismatch during glacial periods in Antarctica?, Quat. Sci. Rev., 25, 49–62, DOI:10.1016/J.QUASCIREV.2005.06.007, 2006.

Landais, A., Dreyfus, G., Capron, E., Masson-Delmotte, V., Sanchez-Goñi, M. F., Desprat, S., Hoffmann, G., Jouzel, J., Leuenberger, M., and Johnsen, S.: What drives the millennial and orbital variations of $\delta 18Oatm$?, Quat. Sci. Rev., 29, 235–246, DOI:10.1016/J.QUASCIREV.2009.07.005, 2010.

Landais, A., Dreyfus, G., Capron, E., Pol, K., Loutre, M. F., Raynaud, D., Lipenkov, V. Y., Arnaud, L., Masson-Delmotte, V., Paillard, D., Jouzel, J., and Leuenberger, M.: Towards orbital dating of the EPICA Dome C ice core using $\delta O2/N2$, Clim. Past, 8, 191–203, DOI:10.5194/CP-8-191-2012, 2012.

Landais, A., Stenni, B., Masson-Delmotte, V., Jouzel, J., Cauquoin, A., Fourré, E., Minster, B., Selmo, E., Extier, T., Werner, M., Vimeux, F., Uemura, R., Crotti, I., and Grisart, A.: Interglacial Antarctic–Southern Ocean climate decoupling due to moisture source area shifts, Nat. Geosci., 14, 918–923, DOI:10.1038/s41561-021-00856-4, 2021.

Lascu, I., Feinberg, J. M., Dorale, J. A., Cheng, H., and Edwards, R. L.: Age of the Laschamp excursion determined by U-Th dating of a speleothem geomagnetic record from North America, Geology, 44, 139–142, DOI:10.1130/G37490.1, 2016.

Laskar, J., Robutel, P., Joutel, F., Gastineau, M., Correia, A. C. M., and Levrard, B.: A long-term numerical solution for the insolation quantities of the Earth, Astron. Astrophys., 428, 261–285, DOI:10.1051/0004-6361:20041335, 2004.

Laskar, J., Fienga, A., Gastineau, M., and Manche, H.: La2010: a new orbital solution for the long-term motion of the Earth, Astron. Astrophys., 532, A89, DOI:10.1051/0004-6361/201116836, 2011.

1082   Lemieux-Dudon, B., Blayo, E., Petit, J. R., Waelbroeck, C., Svensson, A., Ritz, C., Barnola, J. M., Narcisi, B. M.,
1083   and Parrenin, F.: Consistent dating for Antarctic and Greenland ice cores, Quat. Sci. Rev., 29, 8–20,
1084   DOI:10.1016/J.QUASCIREV.2009.11.010, 2010.

1085   Lemieux-Dudon, B., Bazin, L., Landais, A., Toyé Mahamadou Kele, H., Guillevic, M., Kindler, P., Parrenin, F.,
1086   and Martinerie, P.: Implementation of counted layers for coherent ice core chronology, Clim. Past, 11, 959–978,
1087   DOI:10.5194/CP-11-959-2015, 2015.

1088   Ligtenberg, S. R. M., Helsen, M. M., and Van Den Broeke, M. R.: An improved semi-empirical model for the
1089   densification of Antarctic firn, Cryosphere, 5, 809–819, DOI:10.5194/TC-5-809-2011, 2011.

1090   Lipenkov, V., Candaudap, F., Ravoire, J., Dulac, E., and Raynaud, D.: A new device for the measurement of air
1091   content in polar ice, J. Glaciol., 41, 423–429, DOI:10.3189/S0022143000016294, 1995.

1092   Lipenkov, V. Y., Raynaud, D., Loutre, M. F., and Duval, P.: On the potential of coupling air content and O_2/N_2
1093   from trapped air for establishing an ice core chronology tuned on local insolation, Quat. Sci. Rev., 30, 3280–3289,
1094   DOI:10.1016/J.QUASCIREV.2011.07.013, 2011.

1095   Loulergue, L., Schilt, A., Spahni, R., Masson-Delmotte, V., Blunier, T., Lemieux, B., Barnola, J. M., Raynaud,
1096   D., Stocker, T. F., and Chappellaz, J.: Orbital and millennial-scale features of atmospheric CH_4 over the past
1097   800,000 years, Nature, 453, 383–386, DOI:10.1038/nature06950, 2008.

1098   Lu, Z. T., Schlosser, P., Smethie, W. M., Sturchio, N. C., Fischer, T. P., Kennedy, B. M., Purtschert, R.,
1099   Severinghaus, J. P., Solomon, D. K., Tanhua, T., and Yokochi, R.: Tracer applications of noble gas radionuclides
1100   in the geosciences, Earth Sci. Rev., 138, 196–214, DOI:10.1016/J.EARSCIREV.2013.09.002, 2014.

1101   McManus, J. F., Oppo, D. W. and Cullen, J. L., A 0.5-Million-Year Record of Millennial-Scale Climate Variability
1102   in the North Atlantic, Science, 283, 5404, 971-975, DOI:10.1126/science.283.5404.971, 1999.

1103   Moseley, G. E., Spötl, C., Brandstätter, S., Erhardt, T., Luetscher, M., and Lawrence Edwards, R.: NALPS19: Sub-
1104   orbital-scale climate variability recorded in northern Alpine speleothems during the last glacial period, Clim. Past,
1105   16, 29–50, DOI:10.5194/CP-16-29-2020, 2020.

1106   Nehrbass-Ahles, C., Shin, J., Schmitt, J., Bereiter, B., Joos, F., Schilt, A., Schmidely, L., Silva, L., Teste, G., Grilli,
1107   R., Chappellaz, J., Hodell, D., Fischer, H., and Stocker, T. F.: Abrupt CO_2 release to the atmosphere under glacial
1108   and early interglacial climate conditions, Science, 369, 1000–1005, DOI:10.1126/SCIENCE.AAY8178, 2020.

1109   Nye J.F., The motion of ice sheets and glaciers, J. glaciol., 3, 493-507, DOI:10.3189/S002214300001724X, 1959.

1110   Oraschewski, F. M. and Grinsted, A.: Modeling enhanced firn densification due to strain softening, Cryosphere,
1111   16, 2683–2700, DOI:10.5194/TC-16-2683-2022, 2022.

1112   Oyabu, I., Kawamura, K., Buizert, C., Parrenin, F., Orsi, A., Kitamura, K., Aoki, S., and Nakazawa, T.: The Dome
1113   Fuji ice core DF2021 chronology (0–207 kyr BP), Quat. Sci. Rev., 294, 107754,
1114   DOI:10.1016/J.QUASCIREV.2022.107754, 2022.

1115   Parrenin, F., Rémy, F., Ritz, C., Siegert, M. J., and Jouzel, J.: New modeling of the Vostok ice flow line and
1116   implication for the glaciological chronology of the Vostok ice core, J. Geophys. Res. Atmos., 109, D20102,
1117   DOI:10.1029/2004JD004561, 2004.

1118   Parrenin, F., Dreyfus, G., Durand, G., Fujita, S., Gagliardini, O., Gillet, F., Jouze, J., Kawamura, K., Lhomme, N.,
1119   Masson-Delmotte, V., Ritz, C., Schwander, J., Shoji, H., Uemura, R., Watanabe, O., and Yoshida, N.: 1-D-ice
1120   flow modelling at EPICA Dome C and Dome Fuji, East Antarctica, Clim. Past, 3, 243–259, DOI:10.5194/CP-3-
1121   243-2007, 2007a.

1122   Parrenin, F., Barnola, J.-M., Beer, J., Blunier, T., Castellano, E., Chappellaz, J., Dreyfus, G., Fischer, H., Fujita,
1123   S., Jouzel, J., Kawamura, K., Lemieux-Dudon, B., Loulergue, L., Masson-Delmotte, V., Narcisi, B., Petit, J.-R.,
1124   Raisbeck, G., Raynaud, D., Ruth, U., Schwander, J., Severi, M., Spahni, R., Steffensen, J. P., Svensson, A., Udisti,

R., Waelbroeck, C., and Wolff, E.: The EDC3 chronology for the EPICA Dome C ice core, Clim. Past, 3, 485–497, DOI:10.5194/cp-3-485-2007, 2007b.

Parrenin, F., Barker, S., Blunier, T., Chappellaz, J., Jouzel, J., Landais, A., Masson-Delmotte, V., Schwander, J., and Veres, D.: On the gas-ice depth difference (Δdepth) along the EPICA Dome C ice core, Clim. Past, 8, 1239–1255, DOI:10.5194/CP-8-1239-2012, 2012.

Parrenin, F., Bazin, L., Capron, E., Landais, A., Lemieux-Dudon, B., Masson-Delmotte, V., Parrenin, F., Bazin, L., Capron, E., Landais, A., Lemieux-Dudon, B., and Masson-Delmotte, V.: IceChrono1: a probabilistic model to compute a common and optimal chronology for several ice cores, Geosci. Model Dev., 8, 1473–1492, DOI:10.5194/GMD-8-1473-2015, 2015.

Parrenin, F., Bazin, L., Capron, É., Landais, A., Lemieux-Dudon, B., and Masson-Delmotte, V.: Icechrono1 : un modèle probabiliste pour calculer une chronologie commune et optimale pour plusieurs carottes de glace, Quaternaire, 28, 179–184, DOI:10.4000/QUATERNAIRE.8121, 2017.

Parrenin, F., Bazin, L., Buizert, C., Capron, E., Chowdry Beeman, J., Corrick, E., Drysdale, R., Kawamura, K., Landais, A., Mulvaney, R., Oyabu, I., and Rasmussen, S.: The Paleochrono probabilistic model to derive a consistent chronology for several paleoclimatic sites, EGUGA, EGU21-822, DOI:10.5194/EGUSPHERE-EGU21-822, 2021b.

Petit, J. R., Jouzel, J., Raynaud, D., Barkov, N. I., Barnola, J. M., Basile, I., Bender, M., Chappellaz, J., Davis, M., Delaygue, G., Delmotte, M., Kotiyakov, V. M., Legrand, M., Lipenkov, V. Y., Lorius, C., Pépin, L., Ritz, C., Saltzman, E., and Stievenard, M.: Climate and atmospheric history of the past 420,000 years from the Vostok ice core, Antarctica, Nature, 399, 429–436, DOI:10.1038/20859, 1999.

Pimienta, P. and Duval, P.: Rate controlling processes in the creep of polar glacier ice, Journal de Physique Colloques, 48, DOI:10.1051/jphyscol:1987134, 1987.

Raisbeck, G. M., Yiou, F., Jouzel, J., and Stocker, T. F.: Direct north-south synchronization of abrupt climate change record in ice cores using Beryllium 10, Clim. Past, 3, 541–547, DOI:10.5194/CP-3-541-2007, 2007.

Raisbeck, G. M., Cauquoin, A., Jouzel, J., Landais, A., Petit, J. R., Lipenkov, V. Y., Beer, J., Synal, H. A., Oerter, H., Johnsen, S. J., Steffensen, J. P., Svensson, A., and Yiou, F.: An improved north-south synchronization of ice core records around the 41kyr 10Be peak, Clim. Past, 13, 217–229, DOI:10.5194/CP-13-217-2017, 2017.

Raynaud, D., Lipenkov, V., Lemieux-Dudon, B., Duval, P., Loutre, M. F., and Lhomme, N.: The local insolation signature of air content in Antarctic ice. A new step toward an absolute dating of ice records, Earth Planet. Sci. Lett., 261, 337–349, DOI:10.1016/J.EPSL.2007.06.025, 2007.

Reutenauer, C., Landais, A., Blunier, T., Bréant, C., Kageyama, M., Woillez, M. N., Risi, C., Mariotti, V., and Braconnot, P.: Quantifying molecular oxygen isotope variations during a Heinrich stadial, Clim. Past, 11, 1527–1551, DOI:10.5194/CP-11-1527-2015, 2015.

Sánchez Goñi, M. F., Landais, A., Fletcher, W. J., Naughton, F., Desprat, S., and Duprat, J.: Contrasting impacts of Dansgaard–Oeschger events over a western European latitudinal transect modulated by orbital parameters, Quat. Sci. Rev., 27, 1136–1151, DOI:10.1016/J.QUASCIREV.2008.03.003, 2008.

Schwander, J., Jouzel, J., Hammer, C.U., Petit, J.R., Udisti, R. and Wolff, E., A tentative chronology for the EPICA Dome Concordia Ice Core, Geophys. Res. Lett., 28, 4243-4246, DOI:10.1029/2000GL011981, 2001.

Severinghaus, J. P., Bender, M. L., Keeling, R. F., and Broecker, W. S.: Fractionation of soil gases by diffusion of water vapor, gravitational settling, and thermal diffusion, Geochim. Cosmochim. Acta, 60, 1005–1018, DOI:10.1016/0016-7037(96)00011-7, 1996.

Shackleton, N. J.: The 100,000-year ice-age cycle identified and found to lag temperature, carbon dioxide, and orbital eccentricity, Science, 289, 1897–1902, DOI:10.1126/SCIENCE.289.5486.1897, 2000.

Sigl, M., Fudge, T. J., Winstrup, M., Cole-Dai, J., Ferris, D., McConnell, J. R., Taylor, K. C., Welten, K. C., Woodruff, T. E., Adolphi, F., Bisiaux, M., Brook, E. J., Buizert, C., Caffee, M. W., Dunbar, N. W., Edwards, R., Geng, L., Iverson, N., Koffman, B., Layman, L., Maselli, O. J., McGwire, K., Muscheler, R., Nishiizumi, K., Pasteris, D. R., Rhodes, R. H., and Sowers, T. A.: The WAIS Divide deep ice core WD2014 chronology – Part 2: Annual-layer counting (0–31 ka BP), Clim. Past, 12, 769–786, DOI:10.5194/cp-12-769-2016, 2016.

Simon, Q., Bourlès, D.L., Bassinot, F., Nomade, S., Marino, M., Ciaranfi, N., Girone, A., Maiorano, P., Thouveny, N., Choy, S., Dewilde, F., Scao, V., Isguder, G. and Blamart, D., Authigenic 10Be/9Be ratio signature of the Matuyama–Brunhes boundary in the Montalbano Jonico marine succession, Earth Planet. Sci. Lett., 460, 255-267, DOI:10.1016/j.epsl.2016.11.052, 2017.

Suwa, M. and Bender, M. L.: Chronology of the Vostok ice core constrained by O2/N2 ratios of occluded air, and its implication for the Vostok climate records, Quat. Sci. Rev., 27, 1093–1106, DOI:10.1016/J.QUASCIREV.2008.02.017, 2008.

Svensson, A., Andersen, K. K., Bigler, M., Clausen, H. B., Dahl-Jensen, D., Davies, S. M., Johnsen, S. J., Muscheler, R., Parrenin, F., Rasmussen, S. O., Röthlisberger, R., Seierstad, I., Steffensen, J. P., and Vinther, B. M.: A 60 000 year Greenland stratigraphic ice core chronology, Clim. Past, 4, 47–57, DOI:10.5194/CP-4-47-2008, 2008.

Svensson, A., Bigler, M., Blunier, T., Clausen, H. B., Dahl-Jensen, D., Fischer, H., Fujita, S., Goto-Azuma, K., Johnsen, S. J., Kawamura, K., Kipfstuhl, S., Kohno, M., Parrenin, F., Popp, T., Rasmussen, S. O., Schwander, J., Seierstad, I., Severi, M., Steffensen, J. P., Udisti, R., Uemura, R., Vallelonga, P., Vinther, B. M., Wegner, A., Wilhelms, F., and Winstrup, M.: Direct linking of Greenland and Antarctic ice cores at the Toba eruption (74 ka BP), Clim. Past, 9, 749–766, DOI:10.5194/CP-9-749-2013, 2013.

Svensson, A., Dahl-Jensen, D., Steffensen, J. P., Blunier, T., Rasmussen, S. O., Vinther, B. M., Vallelonga, P., Capron, E., Gkinis, V., Cook, E., Kjær, H. A., Muscheler, R., Kipfstuhl, S., Wilhelms, F., Stocker, T. F., Fischer, H., Adolphi, F., Erhardt, T., Sigl, M., Landais, A., Parrenin, F., Buizert, C., McConnell, J. R., Severi, M., Mulvaney, R., and Bigler, M.: Bipolar volcanic synchronization of abrupt climate change in Greenland and Antarctic ice cores during the last glacial period, Clim. Past, 16, 1565–1580, DOI:10.5194/cp-16-1565-2020, 2020.

Tian, L., Ritterbusch, F., Gu, J. Q., Hu, S. M., Jiang, W., Lu, Z. T., Wang, D., and Yang, G. M.: 81Kr Dating at the Guliya Ice Cap, Tibetan Plateau, Geophys. Res. Lett., 46, 6636–6643, DOI:10.1029/2019GL082464, 2019.

Uemura, R., Motoyama, H., Masson-Delmotte, V., Jouzel, J., Kawamura, K., Goto-Azuma, K., Fujita, S., Kuramoto, T., Hirabayashi, M., Miyake, T., Ohno, H., Fujita, K., Abe-Ouchi, A., Iizuka, Y., Horikawa, S., Igarashi, M., Suzuki, K., Suzuki, T., and Fujii, Y.: Asynchrony between Antarctic temperature and CO2 associated with obliquity over the past 720,000 years, Nat. Commun., 9, 1–11, DOI:10.1038/s41467-018-03328-3, 2018.

Veres, D., Bazin, L., Landais, A., Toyé Mahamadou Kele, H., Lemieux-Dudon, B., Parrenin, F., Martinerie, P., Blayo, E., Blunier, T., Capron, E., Chappellaz, J., Rasmussen, S. O., Severi, M., Svensson, A., Vinther, B., and Wolff, E. W.: The Antarctic ice core chronology (AICC2012): an optimized multi-parameter and multi-site dating approach for the last 120 thousand years, Clim. Past, 9, 1733–1748, DOI:10.5194/cp-9-1733-2013, 2013.

Wolff, E. W., Chappellaz, J., Blunier, T., Rasmussen, S. O., and Svensson, A.: Millennial-scale variability during the last glacial: The ice core record, Quat. Sci. Rev., 29, 2828–2838, DOI:10.1016/J.QUASCIREV.2009.10.013, 2010.

Yan, Y., Bender, M. L., Brook, E. J., Clifford, H. M., Kemeny, P. C., Kurbatov, A. v., Mackay, S., Mayewski, P. A., Ng, J., Severinghaus, J. P., and Higgins, J. A.: Two-million-year-old snapshots of atmospheric gases from Antarctic ice, Nature, 574, 663–666, DOI:10.1038/s41586-019-1692-3, 2019.

Yiou, F., Raisbeck, G. M., Baumgartner, S., Beer, J., Hammer, C., Johnsen, S., Jouzel, J., Kubik, P. W., Lestringuez, J., Stiévenard, M., Suter, M., and Yiou, P.: Beryllium 10 in the Greenland Ice Core Project ice core at Summit, Greenland, J. Geophys. Res. Oceans, 102, 26783–26794, DOI:10.1029/97JC01265, 1997.

1213 Zappala, J. C., Baggenstos, D., Gerber, C., Jiang, W., Kennedy, B. M., Lu, Z. T., Masarik, J., Mueller, P.,
1214 Purtschert, R., and Visser, A.: Atmospheric 81Kr as an Integrator of Cosmic-Ray Flux on the Hundred-Thousand-
1215 Year Time Scale, Geophys. Res. Lett., 47, e2019GL086381, DOI:10.1029/2019GL086381, 2020.

1216 Zhao, X., Cheng, H., Sinha, A., Zhang, H., Baker, J. L., Chen, S., Kong, X., Wang, Y., Edwards, R. L., Ning, Y.,
1217 and Zhao, J.: A High-Resolution Speleothem Record of Marine Isotope Stage 11 as a Natural Analog to Holocene
1218 Asian Summer Monsoon Variations, Geophys. Res. Lett., 46, 9949–9957, DOI:10.1029/2019GL083836, 2019.